Inducing topological flat bands in bilayer graphene with electric and magnetic superlattices

Daniel Seleznev [1,*] Jennifer Cano [2,3] and David Vanderbilt [1]

[1]*Department of Physics and Astronomy, Center for Materials Theory, Rutgers University, Piscataway, New Jersey 08854, USA*
[2]*Department of Physics and Astronomy, Stony Brook University, Stony Brook, New York 11794, USA*
[3]*Center for Computational Quantum Physics, Flatiron Institute, New York, New York 10010, USA*

It was recently argued that Bernal stacked bilayer graphene (BLG) exposed to a two-dimensional superlattice (SL) potential exhibits a variety of intriguing behaviors [Ghorashi *et al.*, Phys. Rev. Lett. **130**, 196201 (2023)]. Chief among them is the appearance of flat Chern bands that are favorable to the appearance of fractional Chern insulator states. Here, we explore the application of spatially periodic out-of-plane orbital magnetic fields to the model of Ghorashi *et al.* to find additional means of inducing flat Chern bands. We focus on fields that vary on length scales much larger than the atomic spacing in BLG, generating what we refer to as magnetic SLs. The magnetic SLs we investigate either introduce no net magnetic flux to the SL unit cell or a single quantum of flux. We find that magnetic SLs acting on their own can induce topological flat bands, but richer behavior, such as the appearance of flat and generic bands with high Chern numbers, can be observed when the magnetic SLs act in conjunction with commensurate electric SLs. Finally, we propose a method of generating unit-flux-quantum magnetic SLs along with concomitant electric SLs. The magnetic SL is generated by periodic arrays of flux vortices originating from type II superconductors, while the electric SL arises due to a magnetic SL-induced charge density on the surface of a magnetoelectric material. Tuning the vortex lattice and the magnetoelectric coupling permits control of both SLs, and we study their effects on the band structure of BLG.

I. INTRODUCTION

The past few years have witnessed much excitement surrounding the field of twisted moiré materials. Beginning with the discovery of Mott insulating [1] and superconducting [2,3] behavior in twisted bilayer graphene (TBG), twisted heterostructures—including those not based on graphene alone—have since revealed themselves as highly tunable platforms capable of generating a rich variety of interaction-driven phenomena [1–41]. Underlying the appearance of correlated electron physics in these systems are flat bands induced by the emergence of spatially modulated interlayer couplings acting on the moiré length scale to quench the kinetic energy [42].

Impeding further progress in the field, however, is the high sensitivity of twisted moiré materials to disorder stemming from twist angle inhomogeneities, lattice relaxation, domain formation, and substrate effects. Collectively, these factors hinder sample reproducibility [43], thus making alternative methods of reproducing moiré flat-band physics highly sought after.

Recently, the authors of Refs. [44–46] demonstrated that gated Bernal stacked bilayer graphene (BLG) exposed to a spatially modulated superlattice (SL) potential provides such an alternative platform, whereby the potential emulates the effect of the moiré interlayer coupling. In particular, Ref. [44] indicated that under experimentally feasible conditions, two

distinct flat band regimes may occur. The first "stack of flat bands" scenario features many topologically trivial almost perfectly flat bands spanning a range of energies relevant to the low-energy Hamiltonian describing the system. The second regime features topologically nontrivial flat bands with nonzero Chern numbers C, including those with $|C| > 1$.

The latter regime is especially interesting as it provides the opportunity to explore the interplay between topology and electronic correlations. In twisted heterostructures, this interplay can lead to the appearance of correlation-induced effects and states such as orbital Chern ferromagnetism and the quantum anomalous Hall effect [9–14], as well as the fractional quantum anomalous Hall effect at fractional fillings [15–20,40,41,47]. Bands with $|C| > 1$ have also been proposed to lead to fractional Chern insulating states without Landau level analogues and to other exotic phenomena [48–60]. Furthermore, it has been argued that topology and interactions may be vital to the emergence of superconductivity in these materials [61–63]. In the case of the SL-exposed BLG (SL-BLG) model of Ref. [44], some of the topologically nontrivial flat bands were shown to potentially host fractional Chern insulating states at fractional fillings. Correlated insulating phases have also been recently claimed to have been observed in this setup [64].

Motivated by the possibility of correlated phases in SL-BLG stemming from topological flat bands, the present paper investigates extensions of the model of Ref. [44] to find additional means of inducing flat Chern bands. We focus on the effects of externally applied out-of-plane magnetic fields, due to their tendency to flatten bands and induce band topology.

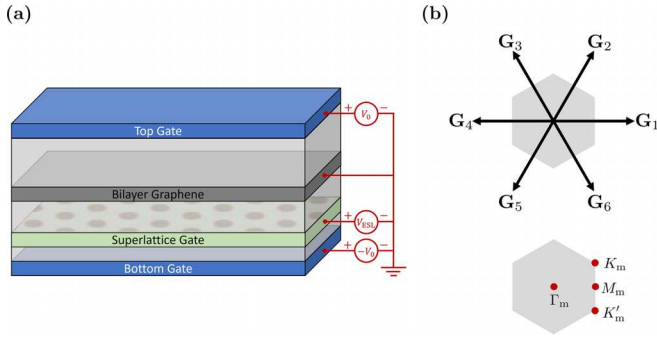*Contact author: dms632@physics.rutgers.edu

205115-1

(a)

(b)

FIG. 1. (a) Schematic depiction of the experimental setup modeled by the SL-BLG Hamiltonian of Ghorashi *et al.* [44]. The system is tuned by a displacement field V_0 and the ESL potential V_{ESL}. (b) Scattering vectors of the triangular ESL of Eq. (5), as well as the corresponding mBZ and its high-symmetry points.

As the model of SL-BLG in Ref. [44] is meant to emulate TBG, we are also motivated to incorporate magnetic fields due to their observed ability to induce interesting correlated behavior in TBG [65–70]. In particular, we study spatially periodic magnetic fields whose variation is on length scales much larger than the intralayer atomic spacing in BLG, generating what we refer to as magnetic SLs (MSLs). Furthermore, we consider two types of MSLs: those that introduce no net magnetic flux to the SL unit cell, and those that introduce a quantum of flux. Due to the size of the SL unit cell, a flux quantum may be realized with magnetic fields on the order of a few Tesla. We find that MSLs on their own can induce topological flat bands, but richer behavior, which can include the appearance of multiple flat and generic (nonflat) bands with high Chern numbers, can be observed when the MSLs act in conjunction with commensurate electric SLs (ESLs).

This paper is organized as follows. In Sec. II, we review the model of SL-BLG introduced in Ref. [44]. In Sec. III we discuss the computational methods we employ to calculate the band structure of SL-BLG exposed to periodic magnetic fields that either do or do not introduce flux to the SL unit cell. Using the methods outlined in the section prior, Sec. IV explores the qualitative impacts of MSLs on SL-BLG using a model of a triangular MSL. In Sec. V, we propose a method of generating MSLs featuring a flux quantum along with concomitant ESLs. The MSL is generated by a periodic array of flux vortices originating from a type II superconductor, while the ESL appears due to an MSL-induced charge density on the surface of a magnetoelectric material. Tuning the vortex lattice and the magnetoelectric coupling permits control of both SLs, and we study their effects on the band structure of BLG. Finally, we summarize the findings of this paper in Sec. VI.

II. BILAYER GRAPHENE EXPOSED TO AN ELECTRIC SUPERLATTICE

In this section we briefly review the model of SL-BLG introduced by Ghorashi *et al.* in Ref. [44]. The suggested experimental setup is depicted schematically in Fig. 1(a), in which the BLG sample is subject to top and bottom gates of equal and opposite voltage, as well as to a spatially varying ESL gate. The latter may be realized in practice by a patterned

dielectric [71], and has been employed in studies of monolayer graphene [71–73]. The BLG exposed to these gates was then modeled by a continuum Hamiltonian,

$$H = H_{\text{BLG}} + H_{V_0} + H_{\text{ESL}}. \tag{1}$$

Because the spin-orbit coupling is extremely weak in BLG, this Hamiltonian may be considered spin degenerate, and we will thus ignore spin labels. The first term on the right-hand side of Eq. (1) describes the low-energy Hamiltonian of intrinsic BLG near the K and K' valleys of the BLG Brillouin zone (BZ) and is given by the four-band Hamiltonian

$$H_{\text{BLG}} = \hbar v \tau^0 (-i\mu \partial_x \sigma^x - i\partial_y \sigma^y) + \frac{t}{2}(\tau^x \sigma^x - \tau^y \sigma^y). \tag{2}$$

Here τ and σ denote Pauli matrices describing the layer and sublattice spaces, respectively, and $\mu = \pm 1$ indicates the K or K' valley.

We take the Fermi velocity to be $v = 10^6$ m/s and adopt $t = 400$ meV as the interlayer hopping between the vertically aligned A and B sublattice sites of the two layers. We shall be interested in energies on the order of tens of meV, i.e., $E \ll t$. In this limit there are two remote high-energy bands near $E = \pm t$, as well as a pair of bands in the low-energy sector that touch quadratically with dispersions $E(\mathbf{k}) = \pm \gamma |\mathbf{k}|^2$ (in the limit of large t), where $\gamma = \hbar^2 v^2 / t$ and $\mathbf{k}$ is defined relative to the K or K' point [74–77].

The displacement field term is given by

$$H_{V_0} = V_0 \tau^z \sigma^0, \tag{3}$$

and applies equal and opposite potential energies on the top and bottom layers. This term opens a gap of size $2|V_0|$ between the low-energy bands, which now disperse as

$$E(\mathbf{k}) = \pm \sqrt{V_0^2 + \gamma^2 |\mathbf{k}|^4}, \tag{4}$$

and as a result are also slightly flattened near $\mathbf{k} = 0$ [74,75,77–80]. In the presence of a nonzero V_0, BLG becomes a valley Chern insulator exhibiting opposite signs of Berry curvature in opposite valleys [76,77,81,82].

The potential term H_{ESL} that is primarily featured in the model of SL-BLG is triangular and symmetric under two-dimensional (2D) inversion (i.e., C_{2z}) and takes the form

$$H_{\text{ESL}} = \frac{V_{\text{ESL}}}{2}[(\tau^0 + \tau^z) + \alpha(\tau^0 - \tau^z)]\sigma^0 \sum_{n=1}^{6} \exp(i\mathbf{G}_n \cdot \mathbf{r}), \tag{5}$$

where $\mathbf{r} = (x, y)$ denotes in-plane position and the $\mathbf{G}_n$ are the scattering wave vectors of the ESL potential. Specifically, $\mathbf{G}_n = Q(\cos \phi_n, \sin \phi_n)$ where $Q = 4\pi/\sqrt{3}L$, $\phi_n = \pi(n - 1)/3$, and L is the SL lattice constant. The $\mathbf{G}_n$ vectors introduce a "mini Brillouin zone" (mBZ) as shown in Fig. 1(b), with its center Γ_m coinciding with the K or K' point of the original BLG BZ. The parameter α is the ratio of SL potentials felt by the top and bottom graphene layers, and takes into account that the top graphene layer is located further away from the SL gate than the bottom layer and experiences a different screening environment. In the rest of this paper, we treat α as a phenomenological parameter and set it to 0.3 [44,83], but we note that it may be computed self-consistently [46].

The ESL potential opens gaps at the mBZ boundaries, and in doing so may generate isolated valley Chern bands. Varying V_0, V_{ESL}, and L then permits control of the band widths as well as their Chern numbers. It is important to note however, that while increasing L will lead to greater band flattening, SLs with large L are also more susceptible to disorder [71]. Additionally, greater L values tend to diminish interband spacings, increasing the sensitivity of band topology to small parameter changes. These considerations must be taken into account when constructing the SL to generate isolated topological bands.

III. BILAYER GRAPHENE EXPOSED TO MAGNETIC SUPERLATTICES

We now turn to a discussion of the calculation of the continuum electronic band structure of SL-BLG exposed to out-of-plane magnetic fields $\mathbf{B}(\mathbf{r})$ that vary on length scales much larger than the atomic spacings in BLG. The fields we consider either introduce no net flux to the SL unit cell, or else a single quantum of flux. For both cases, the minimal coupling prescription introduces the magnetic field $\mathbf{B}(\mathbf{r})$ to the SL-BLG Hamiltonian via the vector potential $\mathbf{A}(\mathbf{r})$, where $\mathbf{B}(\mathbf{r}) = \nabla \times \mathbf{A}(\mathbf{r})$. The vector potential in turn produces an effective periodic scattering potential in both cases. In the presence of a flux quantum, however, it additionally introduces Landau levels (LLs) to the problem. As the magnetic fields we consider are strictly out-of-plane, we will treat them as scalar fields $B(\mathbf{r})$. The electromagnetic gauge can then be chosen so that the vector potential is in-plane: $\mathbf{A}(\mathbf{r}) = [A_x(\mathbf{r}), A_y(\mathbf{r})]$.

The electron spin g factor in BLG is close to 2 [75,84–87] and the magnetic fields we consider are only a few Tesla in strength. (In the case of unit magnetic flux per supercell, we consider superlattice sizes with area about 10 times that of magic-angle TBG, where the corresponding field would be a few tens of Tesla.) As a result, the spin splitting is negligible and we will continue to neglect the spin degree of freedom in the remainder of the paper.

A. Zero net flux magnetic superlattices

When the magnetic field is spatially periodic and introduces no net flux in the periodic domain (unit cell), it can be expressed as a Fourier series without a zeroth harmonic,

$$B(\mathbf{r}) = \sum_{\mathbf{G} \neq 0} B(\mathbf{G}) \exp(i\mathbf{G} \cdot \mathbf{r}), \tag{6}$$

where $B(\mathbf{G})$ denotes a Fourier coefficient. It is then possible to select an electromagnetic gauge in which the vector potential $\mathbf{A}(\mathbf{r})$ shares the same periodicity as $B(\mathbf{r})$:

$$\mathbf{A}(\mathbf{r}) = \sum_{\mathbf{G} \neq 0} \mathbf{A}(\mathbf{G}) \exp(i\mathbf{G} \cdot \mathbf{r}). \tag{7}$$

Note that since we are working with in-plane vector potentials, the Fourier coefficients $\mathbf{A}(\mathbf{G})$ are in-plane as well. As the magnetic field is given by the curl of the vector potential, it is then easy to see that

$$\mathbf{A}(\mathbf{G}) = \frac{B(\mathbf{G}) \hat{\mathbf{z}} \times \mathbf{G}}{i|\mathbf{G}|^2}. \tag{8}$$

The magnetic field is incorporated into the Hamiltonian of Eq. (1) via minimal coupling. In particular, the kinetic energy in Eq. (2) is modified to become

$$\hbar v \tau^0 \left[\mathbf{k} - \frac{e}{\hbar} \mathbf{A}(\mathbf{r}) \right] \cdot \boldsymbol{\sigma}. \tag{9}$$

In the above line, $e < 0$ is the electron charge, $\mathbf{k} = (k_x, k_y) = (-i\partial_x, -i\partial_y)$, $\boldsymbol{\sigma} = (\sigma^x, \sigma^y)$, and we focus on the K valley ($\mu = 1$). Taking advantage of the fact that the kinetic energy is linear in momentum, we may split Eq. (9) into two parts,

$$\hbar v \tau^0 \mathbf{k} \cdot \boldsymbol{\sigma} - ev\tau^0 \mathbf{A}(\mathbf{r}) \cdot \boldsymbol{\sigma}, \tag{10}$$

resulting in the full SL-BLG Hamiltonian of Eq. (1) acquiring an additional term

$$H_{MSL} = -ev\tau^0 \mathbf{A}(\mathbf{r}) \cdot \boldsymbol{\sigma}. \tag{11}$$

In the case of zero net magnetic flux, we may therefore view the periodic magnetic field as generating an effective scattering potential via $\mathbf{A}(\mathbf{r})$ that is superimposed on the one produced by the ESL. Unlike the potential of Eq. (5), however, we note that it now acts to mix the two sublattices.

If we further assume that H_{MSL} is commensurate with H_{ESL}, then the magnetic Hamiltonian remains periodic, just as in the original nonmagnetic case, and the energy eigenstates take the form of Bloch waves, $\psi_{\mathbf{k}}(\mathbf{r}) = e^{i\mathbf{k}\cdot\mathbf{r}} u_{\mathbf{k}}(\mathbf{r})$, where $u_{\mathbf{k}}(\mathbf{r})$ is the cell-periodic Bloch function. Due to the cell-periodicity of $u_{\mathbf{k}}(\mathbf{r})$, all Bloch waves are expressible as superpositions of plane waves, and so we diagonalize the Hamiltonian using the latter. Numerically, convergence of the resulting band structure is ensured by selecting a sufficiently high momentum cutoff for the plane waves.

The Chern number C of an isolated band n is computed from the $\mathbf{k}$-space Berry curvature

$$\Omega_n(\mathbf{k}) = -2\,\mathrm{Im}\langle \partial_x u_{n\mathbf{k}} | \partial_y u_{n\mathbf{k}} \rangle, \tag{12}$$

where $\partial_i = \partial/\partial k_i$. An integration of $\Omega_n(\mathbf{k})$ over the mBZ then yields the Chern number as

$$C = \frac{1}{2\pi} \int_{mBZ} \Omega_n(\mathbf{k})\, d^2k. \tag{13}$$

Numerically, we compute C by tiling the mBZ with plaquettes of sufficiently small size and summing the discretized Berry phases around the boundary of each plaquette [88].

B. Magnetic superlattices with a quantum of flux

When a net magnetic flux permeates the SL unit cell, Eq. (6) is modified by the addition of a zeroth harmonic term, so that

$$B(\mathbf{r}) = B_\Phi + \sum_{\mathbf{G} \neq 0} B(\mathbf{G}) \exp(i\mathbf{G} \cdot \mathbf{r}), \tag{14}$$

where B_Φ is a constant. By superposition, the vector potential corresponding to this magnetic field can then be expressed as

$$\mathbf{A}(\mathbf{r}) = \mathbf{A}_\Phi(\mathbf{r}) + \sum_{\mathbf{G} \neq 0} \mathbf{A}(\mathbf{G}) \exp(i\mathbf{G} \cdot \mathbf{r}). \tag{15}$$

$\mathbf{A}_\Phi(\mathbf{r})$ is taken to be a linear function of position, as in the Landau or symmetric gauge, to generate a uniform B_Φ. The second term, which we will denote as $\mathbf{A}_0(\mathbf{r})$, is the same as

that of Eq. (7), with the Fourier coefficients $\mathbf{A}(\mathbf{G})$ given by the formula of Eq. (8).

Under the minimal coupling scheme, the kinetic energy in Eq. (2) reads

$$\hbar v \tau^0 \left[\mathbf{k} - \frac{e}{\hbar} \mathbf{A}_\Phi(\mathbf{r}) \right] \cdot \boldsymbol{\sigma} + H_{\text{MSL}}, \tag{16}$$

where $H_{\text{MSL}} = -ev\tau^0 \mathbf{A}_0(\mathbf{r}) \cdot \boldsymbol{\sigma}$. We thus see that the periodic piece $\mathbf{A}_0(\mathbf{r})$ of the full vector potential again generates an effective scattering potential, and we will restrict our considerations to MSLs that are commensurate with the ESL. The resulting minimally coupled Hamiltonian therefore describes the low-energy electrons of BLG as being subject to an effective scattering potential $H_{\text{SL}} = H_{\text{ESL}} + H_{\text{MSL}}$, a displacement field, and a constant out-of-plane magnetic field B_Φ. The presence of the latter, however, ultimately results in the Hamiltonian losing its periodicity.

Nonetheless, under certain conditions it is still possible to generate a band structure for this Hamiltonian; we shall now briefly outline the reasons. For more thorough expositions on the subject of band structures in the presence of orbital magnetic fields, we refer the reader to Refs. [89–104].

Under the action of a translation operator $T_{\mathbf{R}} = e^{i\mathbf{p}\cdot\mathbf{R}/\hbar}$, where $\mathbf{R}$ is any nonzero lattice vector, the magnetic Hamiltonian (which now incorporates B_Φ and all scattering terms) is generally not left invariant, since $\mathbf{A}_\Phi(\mathbf{r}) \neq \mathbf{A}_\Phi(\mathbf{r} + \mathbf{R})$ in general. As $\mathbf{A}_\Phi(\mathbf{r})$ is a linear function of position, however, $\mathbf{A}_\Phi(\mathbf{r} + \mathbf{R})$ must generate the same magnetic field B_Φ, and so must be related to $\mathbf{A}_\Phi(\mathbf{r})$ via a gauge transformation,

$$\mathbf{A}_\Phi(\mathbf{r} + \mathbf{R}) = \mathbf{A}_\Phi(\mathbf{r}) + \nabla\phi_{\mathbf{R}}(\mathbf{r}), \tag{17}$$

with $\nabla\phi_{\mathbf{R}}(\mathbf{r}) = \mathbf{A}_\Phi(\mathbf{r} + \mathbf{R}) - \mathbf{A}_\Phi(\mathbf{r})$. $\nabla\phi_{\mathbf{R}}(\mathbf{r})$ must therefore be independent of $\mathbf{r}$, resulting in $\phi_{\mathbf{R}}(\mathbf{r})$ being linear in $\mathbf{r}$. By the same token, $\nabla\phi_{\mathbf{R}}(\mathbf{r})$ is linear in $\mathbf{R}$. The specific form of $\phi_{\mathbf{R}}(\mathbf{r})$ is determined by the choice of gauge for $\mathbf{A}_\Phi(\mathbf{r})$.

The magnetic Hamiltonian is then found to be invariant under the action of the magnetic translation operator

$$\widetilde{T}_{\mathbf{R}} = e^{i\phi_{\mathbf{R}}(\mathbf{r})} T_{\mathbf{R}}. \tag{18}$$

Letting $\widetilde{T}_1$ and $\widetilde{T}_2$ denote the magnetic translation operators corresponding to translations by the unit cell vectors $\mathbf{a}_1$ and $\mathbf{a}_2$, respectively, it can be shown that generally these operators do not commute, with

$$\widetilde{T}_1 \widetilde{T}_2 = e^{2\pi i \Phi/\Phi_0} \widetilde{T}_2 \widetilde{T}_1, \tag{19}$$

where $\Phi = B_\Phi |\mathbf{a}_1 \times \mathbf{a}_2|$ is the flux through the nonmagnetic unit cell and $\Phi_0 = h/|e|$ is the flux quantum. When an integer number of flux quanta pierce the unit cell, the magnetic translation operators do commute, and it is possible to generate a band structure. If instead $\Phi/\Phi_0 = p/q$ where p and q are coprime, then the unit cell must be enlarged q times along one of the lattice vectors to generate a new magnetic cell with p flux quanta. Each band of the $\mathbf{A}_\Phi(\mathbf{r}) = 0$ Hamiltonian is then split into q subbands upon inclusion of B_Φ. Finally, when Φ/Φ_0 is an irrational number, no band structure may be obtained and other methods must be used to solve the Hamiltonian [94].

Although it is tempting to diagonalize the Hamiltonian in the basis of plane waves, as was done in the case of zero

magnetic flux, this can no longer be done when an integer number of flux quanta penetrate the magnetic unit cell. The eigenstates of the magnetic translation operators obey

$$\widetilde{T}_{\mathbf{R}} \psi_{\mathbf{k}}(\mathbf{r}) = e^{i\mathbf{k}\cdot\mathbf{R}} \psi_{\mathbf{k}}(\mathbf{r}), \tag{20}$$

and can always be written in a Bloch-like form as

$$\psi_{\mathbf{k}}(\mathbf{r}) = e^{i\mathbf{k}\cdot\mathbf{r}} u_{\mathbf{k}}(\mathbf{r}). \tag{21}$$

However, in light of $\psi_{\mathbf{k}}(\mathbf{r})$ being an eigenstate of $\widetilde{T}_{\mathbf{R}}$, rather than $T_{\mathbf{R}}$, $u_{\mathbf{k}}(\mathbf{r})$ must obey twisted boundary conditions:

$$u_{\mathbf{k}}(\mathbf{r} + \mathbf{R}) = e^{-i\phi_{\mathbf{R}}(\mathbf{r})} u_{\mathbf{k}}(\mathbf{r}). \tag{22}$$

Due to this fact, the magnetic translation eigenstates cannot be expanded using a plane wave basis.

In the absence of any periodic scattering potential and when $\mathbf{A}_\Phi(\mathbf{r})$ solely generates the magnetic field, the energy eigenstates belong to degenerate LLs. A band structure representation of the energy levels may be obtained by selecting a unit cell with $\Phi = \Phi_0$ and realizing that specific linear combinations of energy eigenstates within a single LL produce energy eigenstates in Bloch form. When a periodic potential is reintroduced to the problem, resulting in a magnetic cell with p flux quanta, each original LL is split into p magnetic subbands. Although states from a single LL no longer form Bloch energy eigenstates, they can be used to construct a basis of magnetic translation eigenstates $|\mathbf{k}, n\rangle$, where $\mathbf{k}$ denotes the wave vector and n indexes the LLs, in which the magnetic Hamiltonian can be diagonalized [89,92,93]. Numerical convergence of the resulting band structure is ensured by a sufficiently high LL cutoff.

The effective kinetic energy in Eq. (16) (first term) can be rewritten in terms of $\boldsymbol{\pi} = \mathbf{p} - e\mathbf{A}_\Phi(\mathbf{r})$, where the components of $\boldsymbol{\pi}$ obey $[\pi_x, \pi_y] = i\hbar e B_\Phi$. The introduction of the ladder operators

$$a = \frac{\pi_x + i\pi_y}{\sqrt{2\hbar e B_\Phi}}, \ a^\dagger = \frac{\pi_x - i\pi_y}{\sqrt{2\hbar e B_\Phi}}, \ [a, a^\dagger] = 1, \tag{23}$$

then allows for straightforward, gauge-independent evaluation of the matrix elements of the kinetic energy in the $|\mathbf{k}, n\rangle$ basis; the matrix elements solely depend on the LL n, and not $\mathbf{k}$. The same cannot be said of the matrix elements of the scattering potential, which further depend on the choice of gauge for the magnetic vector potential.

Reference [100] (see also Supplementary Notes 11 and 12 of Ref. [104] for further discussion) recently demonstrated that the issue of the gauge dependence of the scattering potential matrix elements can be avoided. By expressing the magnetic translation operators via gauge-invariant LL guiding center momenta, and by generating the magnetic translation eigenstates $|\mathbf{k}, n\rangle$ using these operators, the authors derived expressions for the scattering matrix elements that are gauge invariant.

Following the results of this work, for a given scattering potential expressible as a Fourier series with reciprocal lattice vectors $\mathbf{G}$, we compute a matrix element $\langle \mathbf{k}, m | e^{i\mathbf{G}\cdot\mathbf{r}} | \mathbf{k}, n \rangle$ as

$$e^{-i\pi(G_1 G_2 + G_1 + G_2) - 2\pi i(G_1 k_2 - G_2 k_1)} \mathcal{H}_{mn}^{\mathbf{G}}. \tag{24}$$

G_1 and G_2 are the internal coordinates of $\mathbf{G}$, while k_1 and k_2 are those of $\mathbf{k}$. $\mathcal{H}_{mn}^{\mathbf{G}}$ denotes the purely LL-dependent part
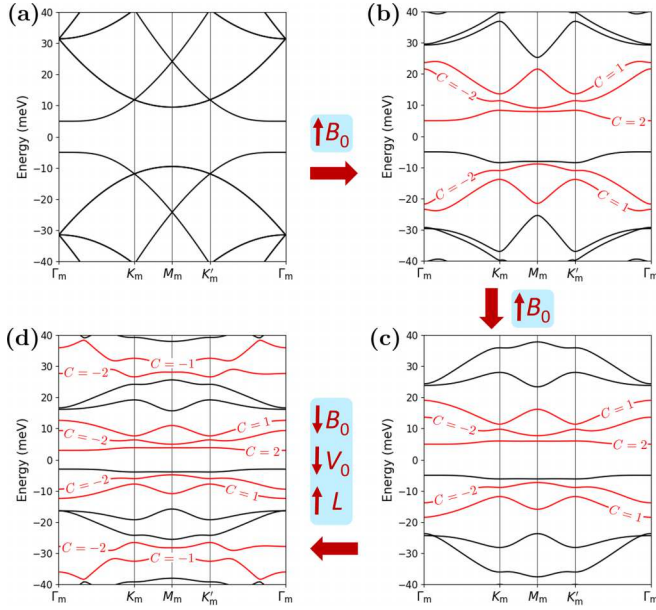
FIG. 2. Evolution of low-energy bands in BLG induced by a triangular MSL, here with zero net flux ($B_\Phi = 0$) and in the absence of the triangular ESL ($V_{ESL} = 0$). The high-symmetry points are defined in Fig. 1(b). (a) Folded bands characterize an empty-lattice starting configuration ($B_0 = 0\,\mathrm{T}$, $V_0 = 5\,\mathrm{meV}$, $L = 40\,\mathrm{nm}$). (b) As B_0 is tuned to 2.5 T, topological bands emerge. (c) Further increasing B_0 to 5 T flattens the bands and produces a flat $C = 2$ band close to the Fermi energy. (d) Decreasing the magnetic field and gate strength while increasing the SL lattice constant ($B_0 = 3\,\mathrm{T}$, $V_0 = 3\,\mathrm{meV}$, $L = 50\,\mathrm{nm}$) introduces more topological bands and further flattens preexisting bands.

TABLE I. Details of flat bands appearing in Fig. 2. Energy at Γ_m, Chern number, band width, gap below, and gap above, respectively (energies in meV).

	E_{Γ_m}	C	W	E_{g-}	E_{g+}
Panel (c)	5.00	2	1.02	9.99	1.75
Panel (d)	3.00	2	0.88	6.00	1.14

number of a band is given by the sum of the LL and character Chern numbers. We employ this method in our calculations.

We note that an alternative approach to computing the Chern numbers involves obtaining the winding numbers of the eigenvalues of appropriately constructed Wilson loops, as shown by Ref. [100]. We confirmed that the Chern numbers computed in this way match those found using the plaquette-based method outlined above.

IV. TRIANGULAR MAGNETIC SUPERLATTICE

In this section we apply the methods described in Sec. III to obtain a qualitative understanding of the effects of MSLs on the band structure of SL-BLG. To this end, we focus on the relatively simple case of a triangular MSL generated by

$$B(\mathbf{r}) = \sum_{n=1}^{6} B_0 \cos(\mathbf{G}_n \cdot \mathbf{r}), \qquad (25)$$

where the reciprocal vectors $\mathbf{G}_n$ are the same as those depicted in Fig. 1(b), and where the field is commensurate with the ESL potential of Eq. (5). We consider both the zero and single flux quantum cases, where the latter is obtained by adding the constant $B_\Phi = (2\Phi_0/\sqrt{3}L^2)$ to $B(\mathbf{r})$. For each flux case, we first study the effect of the magnetic field acting by itself without the ESL, and subsequently study its action in conjunction with the ESL. We find that MSLs acting alone are capable of generating topological flat bands with $|C| = 1$ and 2, but the inclusion of the ESL can further enrich the topology of the band structures by generating an increased number of not only flat, but also generic (nonflat) bands with even higher Chern numbers. In the band structures to be shown, topological bands are highlighted in red. However, we do not highlight those that feature gaps to neighboring bands that are smaller than 0.5 meV, as the topology of these bands is particularly sensitive to changes in model parameters.

We will indicate the topological flat bands in tables corresponding to the band structures. The featured data are Chern numbers C, band widths W, energies at the BZ origin E_{Γ_m}, and energy gaps to the bands immediately below and above, E_{g-} and E_{g+}, respectively. A listed gap value is taken to be the smaller of the indirect or direct gaps; however, in the case when an indirect gap is less than 0.5 meV, we list the smallest direct gap and indicate this fact with a "(D)" next to the gap value. We consider a band to be flat when $W < 2\,\mathrm{meV}$, and will otherwise refer to it as "generic" or "dispersive."

We note that periodic zero-flux fields, including the one we will employ, may in practice be generated by the stray fields of periodic arrays of ferromagnetic nanorods, and have been
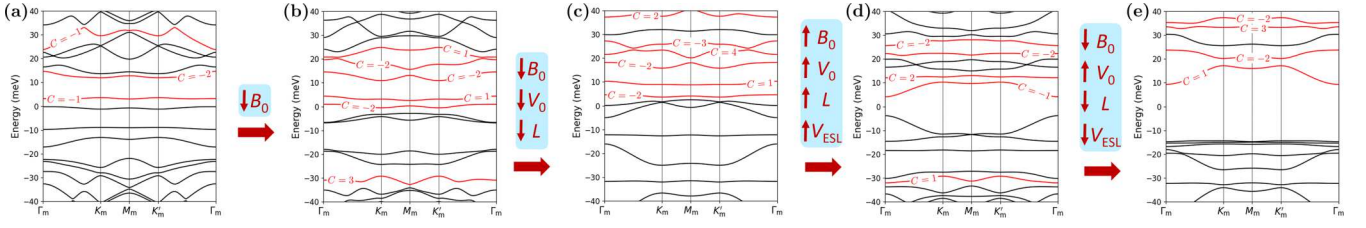
of the scattering amplitude, and is expressed via associated Laguerre polynomials.

We note that the above scattering amplitude is a slight modification of the one explicitly presented in Ref. [100], implementing a suggestion of Herzog-Arbeitman [105]. The modification follows the observation that the original formalism is found to feature an implicit selection of the BZ origin Γ. However, the selected origin may not necessarily be the $\mathbf{k}$-point of maximal symmetry (i.e., the little group of Γ may not equal the point group of the system), and the point of highest symmetry may instead be located elsewhere in the BZ. The scattering amplitude as written in Eq. (24) circumvents this issue to ensure that Γ is the point of highest symmetry. For further details we refer the reader to the Appendix.

The Chern numbers of isolated bands can no longer be computed using the simple plaquette approach outlined previously. A Bloch energy eigenstate at wave vector $\mathbf{k}$ can be expressed as a linear combination $|\psi_{m\mathbf{k}}\rangle = \sum_n \xi_{m\mathbf{k}}(n) |\mathbf{k}, n\rangle$ of the $|\mathbf{k}, n\rangle$ basis states, which themselves represent topologically nontrivial LLs. The Berry curvature at $\mathbf{k}$ therefore arises from two contributions: the Berry curvature of the underlying LLs, and the Berry curvature of the coefficient vectors $\xi_{m\mathbf{k}}$ that give the change in character of the Bloch state in $\mathbf{k}$-space [106,107]. The former contribution is simple, as the Berry curvature of any LL is uniform, and yields a Chern number $C = -1$ [98–100], while the latter contribution can be computed using the plaquette method [106,107]. Thus, the Chern

FIG. 3. Band structures of BLG plotted in the presence of both the triangular ESL and zero-net-flux triangular MSL. (a) $B_0 = 0$ T, $V_{ESL} = 10$ meV, $V_0 = -5$ meV, $L = 50$ nm. (b) $B_0 = -2$ T, $V_{ESL} = 10$ meV, $V_0 = -5$ meV, $L = 50$ nm. (c) $B_0 = -5$ T, $V_{ESL} = 10$ meV, $V_0 = -10$ meV, $L = 44$ nm. (d) $B_0 = 3$ T, $V_{ESL} = 15$ meV, $V_0 = -5$ meV, $L = 50$ nm. (e) $B_0 = -5$ T, $V_{ESL} = 10$ meV, $V_0 = 10$ meV, $L = 45$ nm.

utilized and studied in the context of spintronic applications [108–111].

A. Zero net flux

Throughout this work, we present results for the K valley. Corresponding results for the K' valley can be obtained with an appropriate modification of the parameters. As a reminder, we work in the low-energy regime relative to the scale of interlayer hopping t, so that all of the bands shown emerge from the two low-energy bands of the continuum model of Eq. (4).

Figure 2 depicts the evolution of the band structure as B_0, V_0, and L are varied, while the ESL is absent. Starting with the MSL absent as well ($B_0 = 0$ T, $V_0 = 5$ meV, $L = 40$ nm), turning the MSL on (increasing B_0) lifts the degeneracies at high-symmetry points and along high-symmetry lines in the band structure. Isolated Chern bands appear as B_0 is first increased to 2.5 T, and are subsequently flattened as B_0 is further increased to 5 T. A flat Chern band with $C = 2$ and a band width W on the order of 1 meV then appears close to the Fermi energy, as detailed in Table I. The same band may be further flattened by increasing L to 50 nm, while simultaneously decreasing B_0 and V_0 to 3 T and 3 meV. The increase in lattice constant also introduces more Chern bands into the energy window, though the bands are not necessarily flat. We therefore see that the MSL may introduce flat topological bands, including those with $|C| > 1$, without the ESL. Increasing the field strength reduces band widths, as does increasing the SL size; the latter, however, also increases the density of states and reduces the gaps between isolated bands, potentially increasing the sensitivity of the band topology to changes in model parameters. Barring the emergence of

additional symmetries, accidental degeneracies may also occur between pairs of bands at generic **k**-points as the model parameters are evolved.

We briefly note that although the band structure of Fig. 2(a) is perfectly symmetric about $E = 0$, the band structures in Figs. 2(b)–2(d) are not; this is evident from the Chern numbers of the bands, and closer inspection also reveals asymmetry in the band energies upon reflection about $E = 0$. For a given set of model parameters, the energy spectrum in the K' valley is obtained by reflecting all of the K valley bands about $E = 0$, with the Chern numbers being unchanged by the reflection. As a result, the full two-valley energy spectrum is symmetric about the zero energy.

Next we reintroduce H_{ESL} to the Hamiltonian. Beginning with the magnetic field switched off in Fig. 3(a) (see figure caption for details of the parameters), a $C = -1$ flat band is observed near the Fermi energy, as well as a generic $C = -2$ band [44]. When the magnetic field is turned on ($B_0 = -2$ T) in Fig. 3(b), the number of topological bands belonging to the same energy window increases, with $C = -2$ and $C = 1$ flat bands being found particularly close to the Fermi energy. A band with $C = 3$ can also be observed at lower energies. Further strengthening B_0 while modifying the top and bottom gate voltages and lattice constant, shown in Fig. 3(c), further flattens the $C = -2$ and $C = 1$ bands near the Fermi energy, while also introducing generic bands with high Chern numbers $C = 4$ and $C = -3$. As the magnetic field is diminished in strength and changed in sign while V_{ESL}, V_0, and L are increased in Fig. 3(d), two flat bands with $C = 2$

TABLE II. Details of flat bands appearing in Fig. 3. Energy at Γ_m, Chern number, band width, gap below, and gap above, respectively (energies in meV).

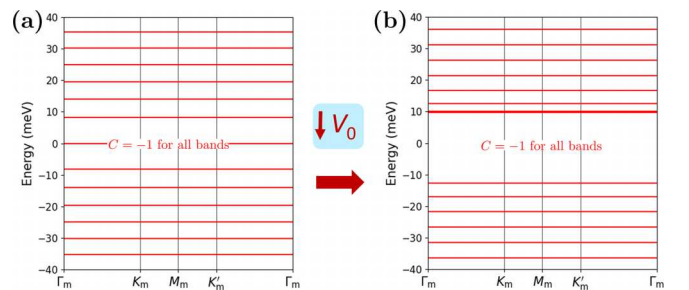|	E_{Γ_m}	C	W	E_{g-}	E_{g+}
Panel (a)	3.20	−1	0.55	3.26	8.34
Panel (b)	0.94	−2	1.46	2.37	1.62
	4.38	1	1.80	1.62	6.57
Panel (c)	4.62	−2	0.96	1.15	4.17
	10.28	1	1.48	4.17	5.55
Panel (d)	12.09	2	0.90	1.82	2.00
	22.29	−2	0.92	1.52	3.23
Panel (e)	33.51	−3	0.87	2.44	1.33

FIG. 4. Band structures of BLG plotted in the presence of the field B_Φ and without any scattering potentials. All bands are perfectly flat with $C = -1$, and directly correspond to LLs. (a) Band structure for $V_0 = 0$. The spectrum is particle-hole symmetric and the bands at $E = 0$ are doubly degenerate. (b) Band structure for $V_0 = -10$. Particle-hole symmetry is broken, and the formerly doubly degenerate bands at $E = 0$ acquire a splitting.
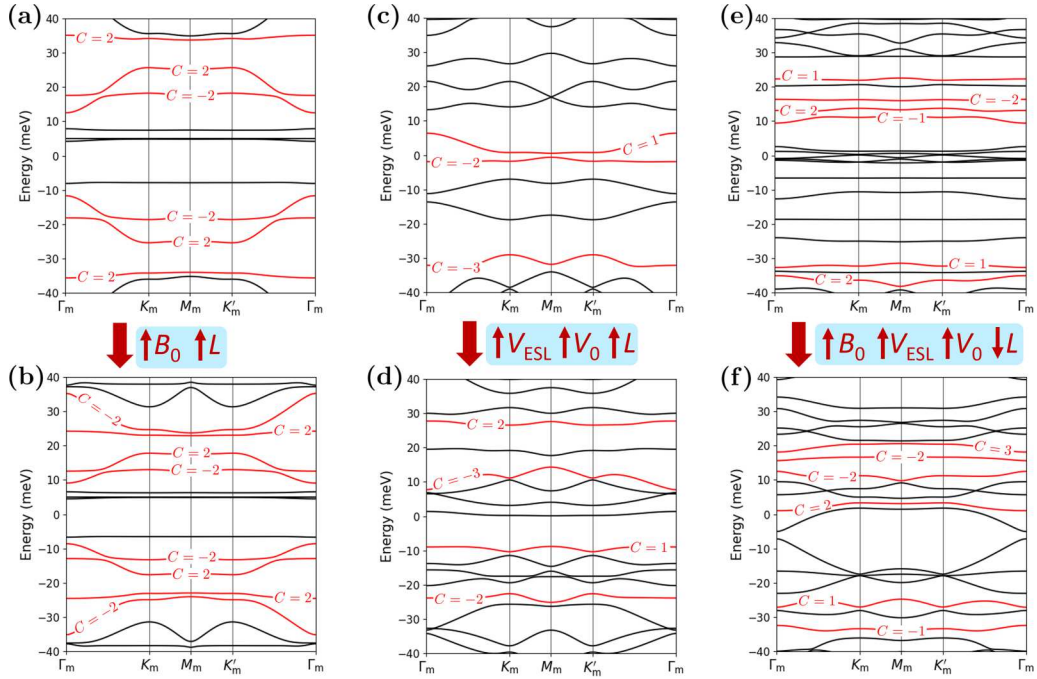
FIG. 5. Band structures of BLG plotted in the presence of the B_Φ background field and one or both of the magnetic or electric triangular SLs. The band structures in panels (a, b) do not feature the ESL ($V_{ESL} = 0$), those in panels (c, d) do not feature the MSL ($B_0 = 0$), while panels (e, f) incorporate both SLs. The specific parameters employed are: (a) $B_0 = -5$ T, $V_{ESL} = 0$ meV, $V_0 = -5$ meV, $L = 40$ nm. (b) $B_0 = -3$ T, $V_{ESL} = 0$ meV, $V_0 = -5$ meV, $L = 50$ nm. (c) $B_0 = 0$ T, $V_{ESL} = 15$ meV, $V_0 = -3$ meV, $L = 40$ nm. (d) $B_0 = 0$ T, $V_{ESL} = 20$ meV, $V_0 = 10$ meV, $L = 50$ nm. (e) $B_0 = -3$ T, $V_{ESL} = 10$ meV, $V_0 = -5$ meV, $L = 60$ nm. (f) $B_0 = 5$ T, $V_{ESL} = 20$ meV, $V_0 = 10$ meV, $L = 51$ nm.

and -2 are found at higher energies. Finally, in Fig. 3(e), another parameter set is found that generates a flat band with $C = 3$ at higher energies, along with other topological bands. Details of the flat bands may be found in Table II.

The detailed nature of these results should not obscure our main point, which is that the addition of the magnetic degree of freedom associated with the strength B_0 of the MSL gives additional opportunities for tuning the system, raising the likelihood of achieving topological flat bands close to the Fermi energy. We additionally note that the qualitative nature of the results is independent of the signs of the model parameters.

B. Single flux quantum

We now consider the case that the background magnetic field B_Φ of Eq. (14) is present, and has been chosen such that the unit cell contains a single flux quantum.

We first plot the magnetic band structures of low-energy continuum BLG in the absence of any periodic scattering potentials; these are just the ordinary LLs of low-energy BLG. Figure 4(a) depicts the band structure in the empty lattice approximation for $L = 50$ nm and $V_0 = 0$ meV. All of the bands are perfectly flat and feature Chern numbers of -1 [95,98]. The bands at $E = 0$ are doubly degenerate; as we are considering the states of BLG originating from the K valley, these LL states are predominantly formed from orbitals on the A sublattice of the bottom layer. For states in the K' valley, the $E = 0$ states are instead formed from orbitals at the B sublattice sites of the top layer [75]. In Fig. 4(b) the displacement field is turned on with $V_0 = -10$ meV. All of the bands retain their original Chern numbers and remain flat,

but are shifted in energy, resulting in broken particle-hole symmetry in the valley. The previously doubly degenerate bands at $E = 0$ are also shifted upwards and feature a small energy splitting [75]. In the opposite K' valley, the energy shifts occur in the opposite direction.

Next we include the effective scattering potentials stemming from the ESL and the inhomogeneous component of the total magnetic field and depict the resulting band structures in Fig. 5 (see figure caption for details of the parameters). Further information on the identified flat bands appears in Table III. We omit flat bands with $|C| = 1$ from the tables, as perfectly flat bands with those Chern numbers can be obtained without employing MSLs. The first column in Fig. 5 depicts band structures with $V_{ESL} = 0$, the middle column those with $B_0 = 0$, while the last column combines both the ESL and

TABLE III. Details of flat bands appearing in Fig. 5. Energy at Γ_m, Chern number, band width, gap below, and gap above, respectively (energies in meV). Flat bands with $|C| = 1$ are omitted.

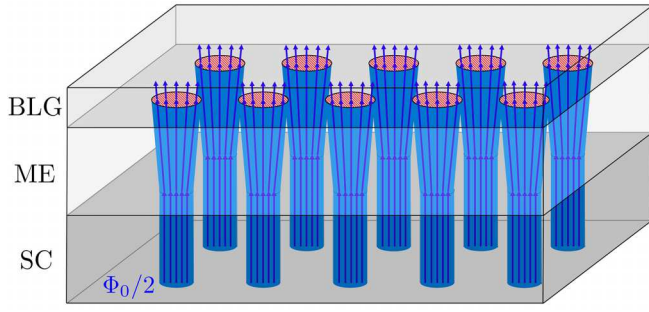|	E_{Γ_m}	C	W	E_{g-}	E_{g+}
Panel (a)	-35.59	2	1.60	1.14 (D)	8.62
	35.12	2	1.38	8.09	1.22 (D)
Panel (b)	24.22	2	1.31	5.12	0.54 (D)
Panel (c)	-1.87	-2	1.28	5.06	1.23
Panel (d)	27.72	2	1.17	6.86	1.96
Panel (e)	13.10	2	0.85	1.36	2.24
	16.36	-2	0.37	2.24	3.70
Panel (f)	15.61	-2	1.19	3.18	1.31

FIG. 6. Schematic depiction of the setup proposed to generate flux quantum MSLs with concomitant ESLs. The MSLs are generated by the magnetic fields (blue lines) emanating from the vortices (blue cylinders) of a mixed state type II superconductor (SC), with each vortex introducing half of a flux quantum $\Phi_0/2$. Prior to penetrating the BLG sample, the magnetic fields pass through a magnetoelectric (ME) material characterized by a ME coupling tensor $\boldsymbol{\alpha}$, inducing a polarization in the bulk and a periodic charge density on the surface. The charge density (red areas) on the surface closest to the BLG generates the ESL potential.

MSL. Starting with the parameters $B_0 = -5$ T, $V_0 = -5$ meV, and $L = 40$ nm, the band structure in Fig. 5(a) exhibits flat bands with $C = 2$ near the top and bottom of the energy window. Other bands with $|C| = 2$ are present as well. As B_0 is weakened to -3 T and the lattice constant is increased to 50 nm [Fig. 5(b)], all band widths are decreased.

Now focusing on the $B_0 = 0$ regime, Fig. 5(c) reveals the appearance of a single flat topological band with $C = -2$ appears close to the Fermi energy, while a $C = -3$ band is present at lower energies. As the ESL potential and the displacement field are strengthened while the SL constant is increased in going to Fig. 5(d), a topological flat band with $C = 2$, as well as generic topological bands with Chern numbers -2 and -3 appear.

When the MSL and ESL are combined in Fig. 5(e), we observe a flat $C = 2$ band, as well as a single particularly flat $C = -2$ band with a bandwidth on the order of 0.4 meV. Subsequently in Fig. 5(f), B_0, V_{ESL}, and V_0 are increased while L is decreased, resulting in an observed $C = -2$ flat band, as indicated in Table III.

We again emphasize that the main point of these results is to demonstrate that the size L of the MSL, in addition to its strength B_0, provide additional degrees of freedom for tuning the system to obtain topological flat bands close to the Fermi energy. We also emphasize that as in Sec. IV A, the qualitative nature of the results is independent of the signs of the model parameters.

V. FLUX QUANTUM MAGNETIC SUPERLATTICES AND CONCOMITANT ELECTRIC SUPERLATTICES

We presently propose a method of generating single-flux-quantum MSLs and concomitant ESLs, for which we envision an experimental setup as illustrated in Fig. 6. The MSL is generated by the magnetic fluxes emanating from the vortices of a type II superconductor in the mixed state. Since we have adopted the notation $\Phi_0 = h/|e|$ for the fundamental flux quantum, each superconducting vortex contributes a flux
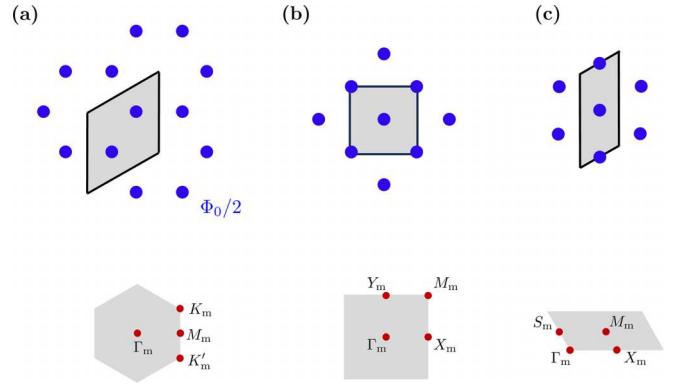

FIG. 7. Magnetic unit cells (top row) and corresponding mBZ domains (bottom row) for the (a) honeycomb, (b) square, and (c) triangular vortex lattices. Each blue dot represents a superconducting flux quantum of $\Phi_0/2$. Panels (a, b) employ the Wigner-Seitz reciprocal lattice cell, with high symmetry points are indicated. Panel (c) shows the primitive reciprocal unit cell and labels points defining the straight-line paths in the mBZ along which the band structures will be plotted.

amount of $h/2|e| = \Phi_0/2$. Thus, a band structure may be generated when the SL unit cell contains an even number of vortices. For simplicity, we model the in-plane profiles of the magnetic fields stemming from individual vortices by isotropic Gaussians. Letting ρ be the width of each Gaussian, the total magnetic field piercing the BLG is then given by

$$B(\mathbf{r}) = \frac{\Phi_0}{2} \sum_{\mathbf{R}, \boldsymbol{\tau}} \frac{\exp[-|\mathbf{r} - \mathbf{R} - \boldsymbol{\tau}|^2/(2\rho^2)]}{2\pi \rho^2}, \quad (26)$$

where $\mathbf{R}$ denotes the origins of unit cells and $\boldsymbol{\tau}$ indicates the basis (locations of vortex centers relative to the origin of a unit cell). We emphasize that Eq. (26) models the magnetic field located inside the BLG, and not the superconductor; hence ρ describes the Gaussian profiles located in the former. In the limit of large ρ, $B(\mathbf{r})$ approaches the homogeneous value of Φ_0/A, where A is the cell area, and we recover the ordinary LL band structure.

In the scenario envisioned in Fig. 6, the concomitant ESL stems from the periodic surface charge density $\sigma(\mathbf{r})$ induced by placing a magnetoelectric material above the superconductor. The vortex magnetic fields penetrating the magnetoelectric induce columns of electric polarization, and the latter in turn produce the surface charge density. The surface charge density is then equal to the z component of the polarization,

$$\sigma_{\text{surf}}(\mathbf{r}) = P_z(\mathbf{r}) = \frac{\alpha_{zz}}{\mu_0} B(\mathbf{r}), \quad (27)$$

where α_{zz} is the relevant component of the magnetoelectric coupling tensor. The resulting potential is then obtained from the 2D integral

$$H_{\text{ESL}} = \frac{[(\tau^0 + \tau^z) + \alpha(\tau^0 - \tau^z)]\sigma^0}{2} \int \frac{e\sigma_{\text{surf}}(\mathbf{r}')d^2r'}{4\pi\epsilon_0|\mathbf{r} - \mathbf{r}'|}. \quad (28)$$
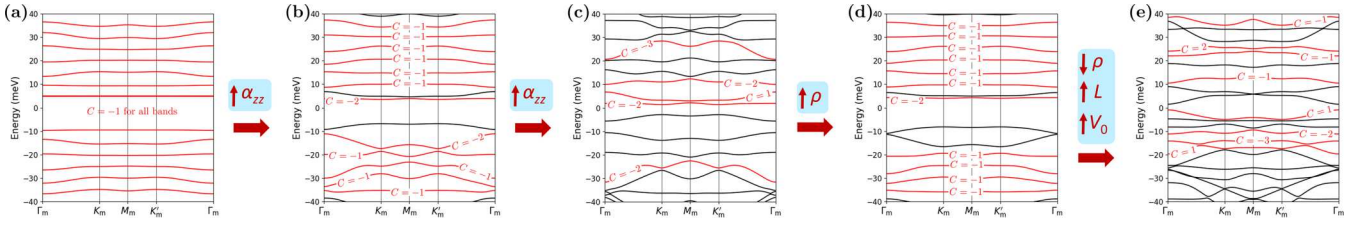
FIG. 8. Band structures of BLG exposed to MSLs and ESLs generated by honeycomb vortex lattices. Starting from a configuration with $\alpha_{zz} = 0\,\mathrm{ps/m}$ (a), the topological characters of the bands are identical to those of LLs. As the ME constant is increased through panels (b) and (c), trivial bands and topological bands with $|C| > 1$ appear. The width ρ is subsequently increased in panel (d), resulting the bands reverting back to LL character. Modifying the other parameters (e) can then result in the appearance of more topological flat bands. The specific parameters employed are: (a) $L = 50\,\mathrm{nm}$, $\rho = 10\,\mathrm{nm}$, $V_0 = -5\,\mathrm{meV}$, $\alpha_{zz} = 0\,\mathrm{ps/m}$. (b) $L = 50\,\mathrm{nm}$, $\rho = 10\,\mathrm{nm}$, $V_0 = -5\,\mathrm{meV}$, $\alpha_{zz} = 30\,\mathrm{ps/m}$. (c) $L = 50\,\mathrm{nm}$, $\rho = 10\,\mathrm{nm}$, $V_0 = -5\,\mathrm{meV}$, $\alpha_{zz} = 80\,\mathrm{ps/m}$. (d) $L = 50\,\mathrm{nm}$, $\rho = 15\,\mathrm{nm}$, $V_0 = -5\,\mathrm{meV}$, $\alpha_{zz} = 80\,\mathrm{ps/m}$. (e) $L = 60\,\mathrm{nm}$, $\rho = 10\,\mathrm{nm}$, $V_0 = 5\,\mathrm{meV}$, $\alpha_{zz} = 80\,\mathrm{ps/m}$.

Employing the convolution theorem and Eq. (27), the ESL potential can then be expressed as

$$H_{\mathrm{ESL}} = [(\tau^0 + \tau^z) + \alpha(\tau^0 - \tau^z)]\sigma^0 \sum_{\mathbf{G} \neq 0} \frac{e\alpha_{zz}c^2}{4|\mathbf{G}|} B(\mathbf{G})e^{i\mathbf{G} \cdot \mathbf{r}},$$
(29)

where c is the speed of light and

$$B(\mathbf{G}) = \frac{\Phi_0}{2A}\left[\sum_{\tau} e^{-i\mathbf{G} \cdot \tau}\right]e^{-|\mathbf{G}|^2\rho^2/2}.$$
(30)

The $\mathbf{G} = 0$ term is omitted from H_{ESL} since the magnetoelectric material is net neutral, with the bottom and top surface charges canceling at large distances. The expression in the brackets corresponds to the structure factor.

In the following, we will consider three types of vortex lattices: honeycomb, square, and triangular, all of which are depicted in Fig. 7. Although triangular vortex lattices are most commonly found in practice, square lattices have been identified in a number of materials [112–116] and proposals for honeycomb lattices have been put forth [117–119]. By studying these three lattices, we aim to identify which structure is most favorable for the emergence of flat topological bands. We consider the vortex spacing to be controllable using temperature or magnetic field strength, and the magnetoelectric constants we will employ belong to the typical range of 0.1 to 100 ps/m. We again emphasize that the detailed nature of the following results is not meant to obscure the main point of this being a highly tunable setup that enables the generation of topological flat bands close to the Fermi energy.

A. Honeycomb vortex lattice

We consider a honeycomb lattice as depicted in Fig. 7(a), with the internal coordinates of the two vortex centers within the unit cell being (1/3, 1/3) and (2/3, 2/3). For this arrangement of vortices, the magnetic cell is identical to the geometric cell.

We track the evolution of the resulting BLG band structure in Fig. 8, which also contains the details of the specific parameters employed. More information on the identified $|C| > 1$ flat bands may be found in Table IV. We initially consider a parameter set with $\alpha_{zz} = 0$ (no ESL) as shown in Fig. 8(a). The resulting bands are all found to be topological, but feature the same Chern numbers as the original BLG LLs. Upon

increasing α_{zz} to 30 ps/m [Fig. 8(b)], several band touchings occur, with band gaps closing and reopening, such that a number of bands become trivial, with a single particularly flat topological band with $C = -2$ emerging near the Fermi energy, as detailed in Table IV. There is also a single generic band with $C = -2$, while all other bands are found to exhibit $C = -1$. Upon further increasing the ME coupling to 80 ps/m [Fig. 8(c)], additional band touchings occur, resulting in more trivial bands, as well as generic bands with higher Chern numbers, including one with $C = -3$. The flat $C = -2$ band close to the Fermi energy remains, but its band width is slightly increased.

Increasing the width ρ of the vortex fields recovers the LL character of many of the bands, as evidenced by Fig. 8(d), although the flat $C = -2$ close to the Fermi energy remains. Subsequently reducing ρ while increasing the cell size L and displacement field V_0 [Fig. 8(e)] introduces more topological flat bands, including those with higher Chern numbers: $C = -3$, -2, and 2. Detailed information on these bands is contained in Table IV.

B. Square vortex lattice

We now turn to the consideration of square flux lattices of the type depicted in Fig. 7(b), with the internal coordinates of the two vortex centers within the unit cell being (0,0) and (1/2, 1/2). Unlike the honeycomb lattice case, the present magnetic cell is twice the size of the geometric cell. The parameter L is now taken to be the lattice constant of the geometric cell, not that of the magnetic cell as was the case in the previous sections.

TABLE IV. Details of flat bands appearing in Fig. 8. Energy at Γ_{m}, Chern number, band width, gap below, and gap above, respectively (energies in meV). Flat bands with $|C| = 1$ are omitted.

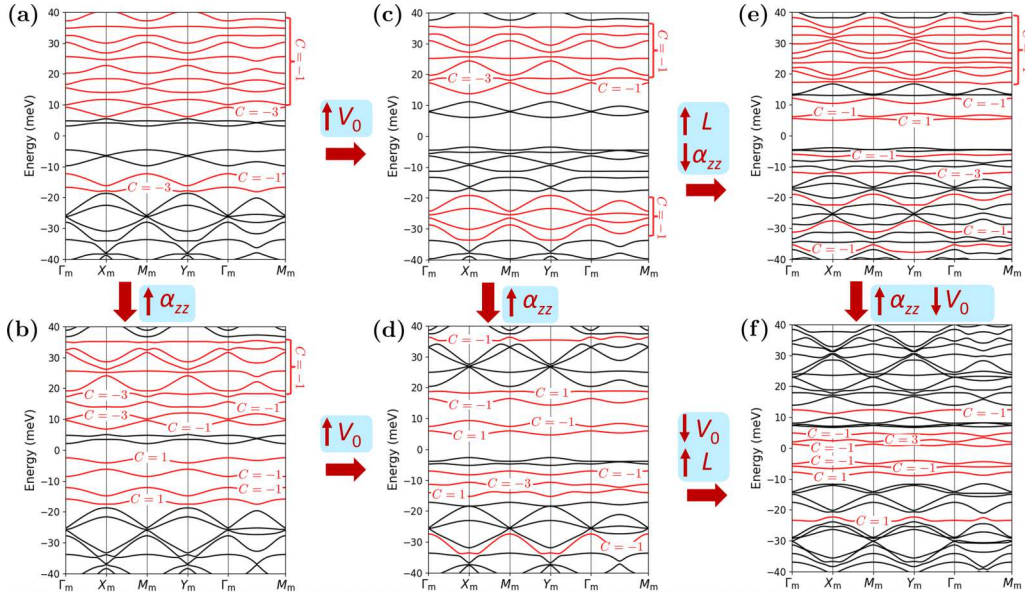|	$E_{\Gamma_{\mathrm{m}}}$	C	W	E_{g-}	E_{g+}
Panel (b)	3.91	-2	0.38	10.32	0.74
Panel (c)	1.90	-2	0.72	4.30	0.87
Panel (d)	4.31	-2	0.31	12.19	0.64
Panel (e)	-14.15	-3	1.40	0.65	2.89
	-11.18	-2	1.70	2.89	0.83
	24.09	2	1.89	1.21 (D)	2.20

FIG. 9. Band structures of BLG exposed to MSLs and ESLs generated by square vortex lattices. All band structures shown employ $\rho = 10$ nm. Panels (a, b) both feature $L = 40$ nm and $V_0 = -5$ meV, with α_{zz} increased from 50 to 80 ps/m in going from panel (a) to panel (b). V_0 is subsequently increased to 5 meV in panels (c, d), with α_{zz} again varying between 50 and 80 ps/m in going from panel (c) to panel (d). In panels (e, f) L is increased to 50 nm, with panel (e) additionally featuring $V_0 = 5$ meV and $\alpha_{zz} = 30$ ps/m, while panel (f) has $V_0 = -5$ meV and $\alpha_{zz} = 80$ ps/m. In the course of varying the parameters, some of the bands retain the Chern numbers of the original LLs, but generic, as well as flat topological bands with $|C| > 1$ may be found near the Fermi energy, or at higher energies.

The evolution of the resulting BLG band structure as a function of the model parameters is depicted in Fig. 9 (see figure caption for parameter values employed), with further flat $|C| > 1$ band details indicated in Table V. In all plots shown, $\rho = 10$ nm. Beginning with Fig. 9(a), we initially consider the case of $L = 40$ nm, $V_0 = -5$ meV, and $\alpha_{zz} = 50$ ps/m. While the majority of the topological bands exhibit $C = -1$, two bands are found to feature $C = -3$, with one of them featuring a band width on the order of 1.5 meV. Increasing α_{zz} to 80 ps/m in Fig. 9(b) results in several band touchings, with an increased number of bands exhibiting $C \neq -1$, and with a flat $C = -3$ band occurring once again.

Figures 9(c) and 9(d) employ the same parameters as Figs. 9(a) and 9(b), respectively, but with $V_0 = 5$ meV. We again find that as α_{zz} is increased from 50 to 80 ps/m in going from Fig. 9(c) to 9(d), a smaller number of bands exhibits the Chern numbers of LLs. In both Figs. 9(c) and 9(d), a $C = -3$ flat band appears.

In going to Figs. 9(e) and 9(f), L is increased to 50 nm. The rest of the parameters in Fig. 9(e) take the values of $V_0 = 5$ meV, $\alpha_{zz} = 30$ ps/m, while in Fig. 9(f) they are $V_0 = -5$ meV and $\alpha_{zz} = 80$ ps/m. Independently of the fact that V_0 changes sign in going between the two band structures, we find that that increasing the ME coupling again results in a smaller number of bands sharing the same Chern numbers as bands representing LLs. There are also topological flat bands with $|C| = 3$ as before, but due to the increase in unit cell size the spacings between the bands are diminished.

A notable feature of the results presented above is that the Chern numbers are all odd integers. Since we start from $C = -1$ in the trivial limit, Fig. 8(a), this means that Chern numbers transfer between bands in units of two when bands touch as parameters are varied. This can be understood from the fact that the unit cell has to be doubled to accommodate a single quantum of flux, and will also be observed in the results presented in the next subsection.

C. Triangular vortex lattice

The triangular vortex lattice and our chosen magnetic unit cell are depicted in Fig. 7(c), with vortex centers located at $(1/2, 0)$ and $(1/2, 1/2)$ in internal coordinates. By L we again denote the geometric rather than magnetic cell lattice constant, and note that as in the square vortex lattice case earlier, the magnetic unit cell is twice the size of the geometric cell.

Band structures as a function of the model parameters are shown in Fig. 10 (see figure caption for parameter details), with Table VI giving some details of selected bands shown in the figure. Starting with $L = 40$ nm, $\rho = 10$ nm, $V_0 = -5$ meV, and $\alpha_{zz} = 50$ ps/m [Fig. 10(a)], we find that most of the bands retain LL topology, with Chern numbers

TABLE V. Details of flat bands appearing in Fig. 9. Energy at Γ_m, Chern number, band width, gap below, and gap above, respectively (energies in meV). Flat bands with $|C| = 1$ are omitted.

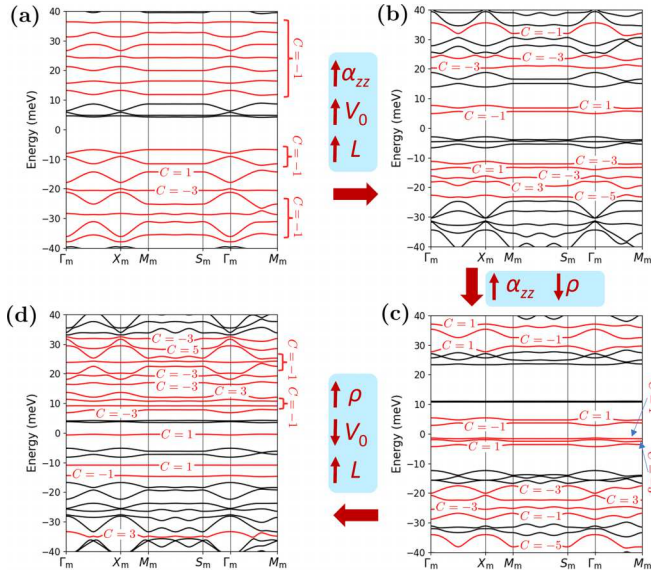|	E_{Γ_m}	C	W	E_{g-}	E_{g+}
Panel (a)	-16.75	-3	1.50	0.79 (D)	0.63
Panel (b)	17.28	-3	0.99	1.88	0.78
Panel (c)	19.70	-3	0.63	1.07	0.90
Panel (d)	-11.40	-3	1.51	0.75	2.47
Panel (e)	-11.90	-3	0.49	0.71	0.88
Panel (f)	1.97	3	1.26	0.80	0.59

FIG. 10. Band structures of BLG exposed to MSLs and ESLs generated by triangular vortex lattices. (a) In the initial configuration with $L = 40$ nm, $\rho = 10$ nm, $V_0 = -5$ meV, and $\alpha_{zz} = 50$ ps/m, the majority of the bands share the topology of the LLs. (b) The increase of L, V_0, and α_{zz} to values of 45 nm, 5 meV, and 80 ps/m, respectively, is marked by the appearance of multiple topological flat bands, including one with $C = -5$. Decreasing ρ to 8 nm, while increasing α_{zz} to 100 ps/m in panel (c) also results in the appearance of a number of topological flat bands, as well as generic bands with $|C| > 1$. Finally panel (d), increasing L and ρ to 50 and 10 nm, respectively, while decreasing V_0 and α_{zz} to -5 meV and 80 ps/m, also yields nontrivial flat bands.

TABLE VI. Details of flat bands appearing in Fig. 10. Energy at Γ_m, Chern number, band width, gap below, and gap above, respectively (energies in meV). Flat bands with $|C| = 1$ are omitted.

	E_{Γ_m}	C	W	E_{g-}	E_{g+}
Panel (a)	−20.02	−3	0.53	0.66	2.33
Panel (b)	−22.69	−5	0.91	1.05	2.07
	−16.18	−3	0.81	0.99	2.20
	−11.27	−3	0.92	1.11	4.62
	20.30	−3	1.09	1.56	1.45
	23.84	−3	1.76	1.45	0.64
Panel (c)	−25.52	−3	0.89	1.38	2.14
	−20.77	3	1.52	2.14	0.98
	−1.99	−3	0.71	0.75	0.52 (D)
Panel (d)	−33.39	3	1.92	0.54	0.65 (D)
	6.79	−3	1.10	2.58	1.19
	13.68	3	1.98	0.88 (D)	2.68
	16.41	−3	0.92	2.68	0.92
	18.09	−3	1.36	0.92	0.56
	32.47	−3	1.47	0.89 (D)	0.71

$C = -1$. A single band is found to have $C = 1$, and there is a flat band with $C = -3$, as detailed in Table VI.

Subsequently increasing L, V_0, and α_{zz} (while keeping ρ fixed), results in an increase in the number of bands with $|C| > 1$, with many of them being flat. Remarkably, a flat band with $C = -5$ can be found at lower energies, and several bands with $C = -3$ and band widths on the order of 1 meV are also present.

We subsequently decrease ρ to 8 nm and increase α_{zz} to 100 ps/m while keeping L and V_0 fixed [Fig. 10(c)]. This time there are not as many flat bands with higher Chern numbers, but we do find generic bands with higher Chern numbers, including ones with $C = -5$ and $C = -3$. At lower energies we also encounter two adjacent flat bands with $C = -3$ and $C = 3$.

In Fig. 10(d), $L = 50$ nm, $\rho = 10$ nm, $V_0 = -5$ meV, and $\alpha_{zz} = 80$ ps/m. We find a number of topological flat bands, including a variety of $|C| = 3$ bands of varying band widths and at various energies. A generic $C = -5$ band also appears at higher energies.

VI. SUMMARY

In this paper we have studied the application of MSLs generated by out-of-plane orbital magnetic fields as an additional means of inducing topological flat bands in BLG. We considered MSLs that either introduce no net flux or a quantum

of flux to the SL unit cell. In the latter case, we employed the recently developed gauge-invariant method of Ref. [100] to perform band structure calculations. We also explored the consequences of MSLs acting in conjunction with ESLs on the band structure of BLG.

To obtain a qualitative understanding of the action of MSLs on the BLG band structure, we initially explored the application of a simple triangular MSL in the first-harmonic approximation. When acting by itself, with or without a quantum of flux, the MSL was found to induce topological flat bands of Chern number $|C| > 1$ when the field strength, displacement field voltage and SL lattice constant were varied. Increasing the strength of the field or increasing the SL size was found to consistently reduce band widths. Generic topological bands were also obtained, including those of higher Chern number. Upon introduction of the commensurate triangular ESL primarily studied by Ghorashi *et al.* [44], the topology of the band structures may be enriched, with more topological flat and generic bands appearing. In the flux quantum case particularly, topological flat bands could be more readily induced.

We subsequently proposed a platform for the realization of flux quantum MSLs with concomitant ESL potentials. Our proposed setup involved generating the MSL using superconductor vortex lattices, and exposing a magnetoelectric material to the magnetic fields of the vortex lattice; the subsequently induced commensurate surface charge density generated the ESL potential. We explored this setup and its application to BLG with honeycomb, square, and triangular vortex lattices to identify the structure most amenable to topological flat bands, including those with higher Chern numbers. In all cases, band flatness could be tuned by the SL cell size as well as the width of the in-plane profiles of the magnetic fields in the vortices, although large widths eventually resulted in the recovery of LL topology. Increasing the magnetoelectric constant promoted band gap closings and reopenings, leading to a greater number of bands (flat or generic) with $|C| > 1$. The square and triangular vortex lattices proved to be especially

conducive for the appearance of bands of particularly high Chern numbers; however, the doubling of the magnetic unit cell relative to the geometric unit cell yielded smaller band gaps between neighboring bands.

In the absence of the MSL, the SL-BLG model was demonstrated by Ref. [44] to feature topological bands favorable to the appearance of fractional Chern insulator states. An additional study performed by Ref. [46] indicated the emergence of quantum anomalous Hall states generated by spontaneous valley symmetry breaking. While calculations establishing the appearance of such interaction driven topological states in the presence of MSLs are beyond the scope of the present work, we emphasize that the topological flat bands obtained may be favorable to the appearance of correlated quantum Hall states. Experimentally, the topology of the bands may be detected by gating the system to populate or depopulate the bands; the subsequent measured change in the Hall conductivity would then indicate the Chern numbers of the bands of interest.

APPENDIX: MODIFICATION OF THE MAGNETIC BLOCH STATE SCATTERING AMPLITUDES

As discussed in Sec. III B, we employ a gauge-invariant formalism developed in Ref. [100] to compute the continuum electronic band structures of SL-BLG in the presence of magnetic flux quanta Φ_0. The primary advantage of this formalism is the gauge-invariant evaluation of the scattering matrix elements $\langle \mathbf{k}, m | e^{i\mathbf{G} \cdot \mathbf{r}} | \mathbf{k}, n \rangle$, where $|\mathbf{k}, n\rangle$ is a magnetic translation eigenstate, with $\mathbf{k}$ denoting the wave vector and n indicating the index of the LL used to construct the state. Reference [100] demonstrated that

$$\langle \mathbf{k}, m | e^{i\mathbf{G} \cdot \mathbf{r}} | \mathbf{k}, n \rangle = e^{-i\pi G_1 G_2 - 2\pi i (G_1 k_2 - G_2 k_1)} \mathcal{H}_{mn}^{\mathbf{G}}, \quad \text{(A1)}$$

where G_1 and G_2 are the internal coordinates of $\mathbf{G}$ and k_1 and k_2 are those of $\mathbf{k}$. $\mathcal{H}_{mn}^{\mathbf{G}}$ is a LL-dependent quantity that is expressed in terms of associated Laguerre polynomials.

The gauge-invariant evaluation of the scattering amplitudes is enabled by introducing translation operators written in terms of gauge-invariant LL guiding center momenta $\mathbf{Q}$, defined as

$$\mathbf{Q} = \boldsymbol{\pi} - eB_\Phi \mathbf{r} \times \hat{\mathbf{z}}. \quad \text{(A2)}$$

Here, $\boldsymbol{\pi} = \mathbf{p} - e\mathbf{A}_\Phi(\mathbf{r})$, where $\mathbf{p}$ is the canonical momentum operator, $\mathbf{A}_\Phi(\mathbf{r})$ is the vector potential corresponding to the field B_Φ, and $\mathbf{r} = (x, y, 0)$. The magnetic translation eigenstates $|\mathbf{k}, n\rangle$ are then generated with the help of the
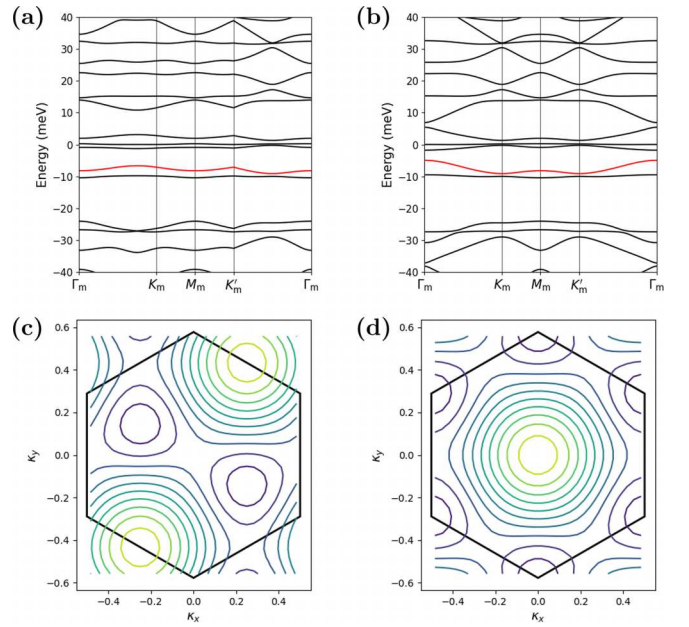

FIG. 11. (a, b) Band structures of the triangular SL lattice model with flux presented in Sec. IV B computed using (a) the original scattering amplitude of Eq. (A1) or (b) the modified scattering amplitude in Eq. (A3). The model parameters are $B_0 = -2\,$T, $V_{\mathrm{ESL}} = 10\,$meV, $V_0 = -5\,$meV, $L = 50\,$nm. (c, d) Contour plots for the band highlighted in red in panels (a, b), respectively. Here $\kappa_i = k_i/Q$, where Q is the reciprocal lattice constant, and the hexagon outlines the Wigner-Seitz mBZ.

translation operators corresponding to primitive translations $T_{\mathbf{a}_i} = \exp(i\mathbf{a}_i \cdot \mathbf{Q}/\hbar)$, and $[T_{\mathbf{a}_1}, T_{\mathbf{a}_2}] = 0$ when an integer number of flux quanta thread the unit cell.

A subtlety of this formalism is the choice of origin of the magnetic BZ. In the case of zero-flux band structures, the BZ origin Γ is the point of highest symmetry in the band structure, and shares the point group symmetry of the system under consideration. The formulation of Herzog-Arbeitman *et al.* [100] features an implicit selection of the BZ origin, but the selected Γ may not be the $\mathbf{k}$-point with maximal symmetry. We see an example of this in Fig. 11(a), in which a band structure of the triangular MSL model of Sec. IV is shown, with a contour plot corresponding to the highlighted red band shown in the panel below. It is clear from the contour plot that Γ_m is not the point of highest symmetry, and in the band structure we find that other high-symmetry points do not have the expected symmetry either. For example, while K_m—a point with threefold rotational symmetry—is expected to feature zero group velocity, it is clear from the plotted band structure that is not the case.

From the contour plot in Fig. 11(a), however, it appears that a rigid translation of the band structure would result in Γ_m becoming the highest symmetry point. A shift of the band structure in $\mathbf{k}$-space may occur by effecting a gauge transformation whereby $\mathbf{A}_\Phi(\mathbf{r}) \rightarrow \mathbf{A}_\Phi(\mathbf{r}) + \mathbf{A}_0$, where $\mathbf{A}_0$ is a constant; under such a transformation, $\mathbf{k} \rightarrow \mathbf{k} - \frac{e}{\hbar} \mathbf{A}_0$. The choice of $\mathbf{A}_0$ is therefore implicit in the formalism of Ref. [100]. To ensure that $\mathbf{A}_0$ is always chosen so that Γ is the highest symmetry point, the scattering amplitude of Eq. (A1)

may be modified to be [105]

$$\langle \mathbf{k}, m | e^{i\mathbf{G}\cdot\mathbf{r}} | \mathbf{k}, n \rangle = e^{-i\pi(G_1 G_2 + G_1 + G_2) - 2\pi i(G_1 k_2 - G_2 k_1)} \mathcal{H}_{mn}^{\mathbf{G}},$$
(A3)

where an additional phase factor of $e^{-i\pi(G_1+G_2)}$ now multiplies the original scattering amplitude. With this modified scattering amplitude we find that the band structure, plotted in Fig. 11(b), now obeys the symmetries of the system. We employ the modified scattering amplitude to calculate all band structures plotted in the main text.

A second subtlety in this formalism arises with the choice of spatial origin of the unit cell relative to the guiding centers. A change in the origin manifests itself in a constant shift of the guiding center momentum operator $\mathbf{Q}$, and in turn modifies the translation operators $T_{\mathbf{a}_i}$ by constant phase factors. These phase factors result in a shift of the $\mathbf{k}$-points and therefore band structure, and thus may again result in Γ not being the point of maximal symmetry in the BZ.

In the case of the triangular MSL model of Sec. IV, the obvious choice of origin centered on the maximum of $B(\mathbf{r})$ automatically ensures the desired symmetry in reciprocal space. For the structures in Sec. V with two vortices per cell, however, we find that we need to take care to make a choice that places the vortices at high-symmetry positions, as other choices result in a violation of the desired $\mathbf{k}$-space symmetry.

[1] Y. Cao, V. Fatemi, A. Demir, S. Fang, S. L. Tomarken, J. Y. Luo, J. D. Sanchez-Yamagishi, K. Watanabe, T. Taniguchi, E. Kaxiras, R. C. Ashoori, and P. Jarillo-Herrero, Correlated insulator behaviour at half-filling in magic-angle graphene superlattices, Nature (London) **556**, 80 (2018).

[2] Y. Cao, V. Fatemi, S. Fang, K. Watanabe, T. Taniguchi, E. Kaxiras, and P. Jarillo-Herrero, Unconventional superconductivity in magic-angle graphene superlattices, Nature (London) **556**, 43 (2018).

[3] M. Yankowitz, S. Chen, H. Polshyn, Y. Zhang, K. Watanabe, T. Taniguchi, D. Graf, A. F. Young, and C. R. Dean, Tuning superconductivity in twisted bilayer graphene, Science **363**, 1059 (2019).

[4] G. Chen, L. Jiang, S. Wu, B. Lyu, H. Li, B. L. Chittari, K. Watanabe, T. Taniguchi, Z. Shi, J. Jung, Y. Zhang, and F. Wang, Evidence of a gate-tunable Mott insulator in a trilayer graphene moiré superlattice, Nat. Phys. **15**, 237 (2019).

[5] E. C. Regan, D. Wang, C. Jin, M. I. Bakti Utama, B. Gao, X. Wei, S. Zhao, W. Zhao, Z. Zhang, K. Yumigeta, M. Blei, J. D. Carlström, K. Watanabe, T. Taniguchi, S. Tongay, M. Crommie, A. Zettl, and F. Wang, Mott and generalized Wigner crystal states in WSe$_2$/WS$_2$ moiré superlattices, Nature (London) **579**, 359 (2020).

[6] T. Li, S. Jiang, L. Li, Y. Zhang, K. Kang, J. Zhu, K. Watanabe, T. Taniguchi, D. Chowdhury, L. Fu, J. Shan, and K. F. Mak, Continuous Mott transition in semiconductor moiré superlattices, Nature (London) **597**, 350 (2021).

[7] G. Chen, A. L. Sharpe, P. Gallagher, I. T. Rosen, E. J. Fox, L. Jiang, B. Lyu, H. Li, K. Watanabe, T. Taniguchi, J. Jung, Z. Shi, D. Goldhaber-Gordon, Y. Zhang, and F. Wang, Signatures of tunable superconductivity in a trilayer graphene moiré superlattice, Nature (London) **572**, 215 (2019).

[8] H. Li, S. Li, E. C. Regan, D. Wang, W. Zhao, S. Kahn, K. Yumigeta, M. Blei, T. Taniguchi, K. Watanabe, S. Tongay, A. Zettl, M. F. Crommie, and F. Wang, Imaging two-dimensional generalized Wigner crystals, Nature (London) **597**, 650 (2021).

[9] A. L. Sharpe, E. J. Fox, A. W. Barnard, J. Finney, K. Watanabe, T. Taniguchi, M. A. Kastner, and D. Goldhaber-Gordon, Emergent ferromagnetism near three-quarters filling in twisted bilayer graphene, Science **365**, 605 (2019).

[10] X. Lu, P. Stepanov, W. Yang, M. Xie, M. A. Aamir, I. Das, C. Urgell, K. Watanabe, T. Taniguchi, G. Zhang, A. Bachtold, A. H. MacDonald, and D. K. Efetov, Superconductors, orbital magnets and correlated states in magic-angle bilayer graphene, Nature (London) **574**, 653 (2019).

[11] M. Serlin, C. L. Tschirhart, H. Polshyn, Y. Zhang, J. Zhu, K. Watanabe, T. Taniguchi, L. Balents, and A. F. Young, Intrinsic quantized anomalous Hall effect in a moiré heterostructure, Science **367**, 900 (2020).

[12] G. Chen, A. L. Sharpe, E. J. Fox, Y.-H. Zhang, S. Wang, L. Jiang, B. Lyu, H. Li, K. Watanabe, T. Taniguchi, Z. Shi, T. Senthil, D. Goldhaber-Gordon, Y. Zhang, and F. Wang, Tunable correlated Chern insulator and ferromagnetism in a moiré superlattice, Nature (London) **579**, 56 (2020).

[13] H. Polshyn, J. Zhu, M. A. Kumar, Y. Zhang, F. Yang, C. L. Tschirhart, M. Serlin, K. Watanabe, T. Taniguchi, A. H. MacDonald, and A. F. Young, Electrical switching of magnetic order in an orbital Chern insulator, Nature (London) **588**, 66 (2020).

[14] C. L. Tschirhart, M. Serlin, H. Polshyn, A. Shragai, Z. Xia, J. Zhu, Y. Zhang, K. Watanabe, T. Taniguchi, M. E. Huber, and A. F. Young, Imaging orbital ferromagnetism in a moiré Chern insulator, Science **372**, 1323 (2021).

[15] Y. Xie, A. T. Pierce, J. M. Park, D. E. Parker, E. Khalaf, P. Ledwith, Y. Cao, S. H. Lee, S. Chen, P. R. Forrester, K. Watanabe, T. Taniguchi, A. Vishwanath, P. Jarillo-Herrero, and A. Yacoby, Fractional Chern insulators in magic-angle twisted bilayer graphene, Nature (London) **600**, 439 (2021).

[16] F. Xu, Z. Sun, T. Jia, C. Liu, C. Xu, C. Li, Y. Gu, K. Watanabe, T. Taniguchi, B. Tong, J. Jia, Z. Shi, S. Jiang, Y. Zhang, X. Liu, and T. Li, Observation of integer and fractional quantum anomalous Hall effects in twisted bilayer MoTe$_2$, Phys. Rev. X **13**, 031037 (2023).

[17] J. Cai, E. Anderson, C. Wang, X. Zhang, X. Liu, W. Holtzmann, Y. Zhang, F. Fan, T. Taniguchi, K. Watanabe, Y. Ran, T. Cao, L. Fu, D. Xiao, W. Yao, and X. Xu, Signatures of fractional quantum anomalous Hall states in twisted MoTe$_2$, Nature (London) **622**, 63 (2023).

[18] H. Park, J. Cai, E. Anderson, Y. Zhang, J. Zhu, X. Liu, C. Wang, W. Holtzmann, C. Hu, Z. Liu, T. Taniguchi, K. Watanabe, J.-H. Chu, T. Cao, L. Fu, W. Yao, C.-Z. Chang, D. Cobden, D. Xiao, and X. Xu, Observation of fractionally quantized anomalous Hall effect, Nature (London) **622**, 74 (2023).

[19] Y. Zeng, Z. Xia, K. Kang, J. Zhu, P. Knüppel, C. Vaswani, K. Watanabe, T. Taniguchi, K. F. Mak, and J. Shan,

Thermodynamic evidence of fractional Chern insulator in moiré MoTe$_2$, Nature (London) **622**, 69 (2023).

[20] Z. Lu, T. Han, Y. Yao, A. P. Reddy, J. Yang, J. Seo, K. Watanabe, T. Taniguchi, L. Fu, and L. Ju, Fractional quantum anomalous Hall effect in multilayer graphene, Nature (London) **626**, 759 (2024).

[21] X. Liu, Z. Hao, E. Khalaf, J. Y. Lee, Y. Ronen, H. Yoo, D. Haei Najafabadi, K. Watanabe, T. Taniguchi, A. Vishwanath, and P. Kim, Tunable spin-polarized correlated states in twisted double bilayer graphene, Nature (London) **583**, 221 (2020).

[22] G. W. Burg, J. Zhu, T. Taniguchi, K. Watanabe, A. H. MacDonald, and E. Tutuc, Correlated insulating states in twisted double bilayer graphene, Phys. Rev. Lett. **123**, 197702 (2019).

[23] M. He, Y. Li, J. Cai, Y. Liu, K. Watanabe, T. Taniguchi, X. Xu, and M. Yankowitz, Symmetry breaking in twisted double bilayer graphene, Nat. Phys. **17**, 26 (2021).

[24] C. Shen, Y. Chu, Q. Wu, N. Li, S. Wang, Y. Zhao, J. Tang, J. Liu, J. Tian, K. Watanabe, T. Taniguchi, R. Yang, Z. Y. Meng, D. Shi, O. V. Yazyev, and G. Zhang, Correlated states in twisted double bilayer graphene, Nat. Phys. **16**, 520 (2020).

[25] Y. Cao, D. Rodan-Legrain, O. Rubies-Bigorda, J. M. Park, K. Watanabe, T. Taniguchi, and P. Jarillo-Herrero, Tunable correlated states and spin-polarized phases in twisted bilayer–bilayer graphene, Nature (London) **583**, 215 (2020).

[26] J. M. Park, Y. Cao, K. Watanabe, T. Taniguchi, and P. Jarillo-Herrero, Tunable strongly coupled superconductivity in magic-angle twisted trilayer graphene, Nature (London) **590**, 249 (2021).

[27] S. Xu, M. M. Al Ezzi, N. Balakrishnan, A. Garcia-Ruiz, B. Tsim, C. Mullan, J. Barrier, N. Xin, B. A. Piot, T. Taniguchi, K. Watanabe, A. Carvalho, A. Mishchenko, A. K. Geim, V. I. Fal'ko, S. Adam, A. H. C. Neto, K. S. Novoselov, and Y. Shi, Tunable van Hove singularities and correlated states in twisted monolayer–bilayer graphene, Nat. Phys. **17**, 619 (2021).

[28] S. Chen, M. He, Y.-H. Zhang, V. Hsieh, Z. Fei, K. Watanabe, T. Taniguchi, D. H. Cobden, X. Xu, C. R. Dean, and M. Yankowitz, Electrically tunable correlated and topological states in twisted monolayer–bilayer graphene, Nat. Phys. **17**, 374 (2021).

[29] Z. Hao, A. M. Zimmerman, P. Ledwith, E. Khalaf, D. H. Najafabadi, K. Watanabe, T. Taniguchi, A. Vishwanath, and P. Kim, Electric field–tunable superconductivity in alternating-twist magic-angle trilayer graphene, Science **371**, 1133 (2021).

[30] Y. Xu, S. Liu, D. A. Rhodes, K. Watanabe, T. Taniguchi, J. Hone, V. Elser, K. F. Mak, and J. Shan, Correlated insulating states at fractional fillings of moiré superlattices, Nature (London) **587**, 214 (2020).

[31] Y. Tang, L. Li, T. Li, Y. Xu, S. Liu, K. Barmak, K. Watanabe, T. Taniguchi, A. H. MacDonald, J. Shan, and K. F. Mak, Simulation of Hubbard model physics in WSe$_2$/WS$_2$ moiré superlattices, Nature (London) **579**, 353 (2020).

[32] L. Wang, E.-M. Shih, A. Ghiotto, L. Xian, D. A. Rhodes, C. Tan, M. Claassen, D. M. Kennes, Y. Bai, B. Kim, K. Watanabe, T. Taniguchi, X. Zhu, J. Hone, A. Rubio, A. N. Pasupathy, and C. R. Dean, Correlated electronic phases in twisted bilayer transition metal dichalcogenides, Nat. Mater. **19**, 861 (2020).

[33] Y. Xu, A. Ray, Y.-T. Shao, S. Jiang, K. Lee, D. Weber, J. E. Goldberger, K. Watanabe, T. Taniguchi, D. A. Muller, K. F. Mak, and J. Shan, Coexisting ferromagnetic–antiferromagnetic state in twisted bilayer CrI$_3$, Nat. Nanotechnol. **17**, 143 (2022).

[34] T. Song, Q.-C. Sun, E. Anderson, C. Wang, J. Qian, T. Taniguchi, K. Watanabe, M. A. McGuire, R. Stöhr, D. Xiao, T. Cao, J. Wrachtrup, and X. Xu, Direct visualization of magnetic domains and moiré magnetism in twisted 2D magnets, Science **374**, 1140 (2021).

[35] O. Can, T. Tummuru, R. P. Day, I. Elfimov, A. Damascelli, and M. Franz, High-temperature topological superconductivity in twisted double-layer copper oxides, Nat. Phys. **17**, 519 (2021).

[36] S. Y. F. Zhao, X. Cui, P. A. Volkov, H. Yoo, S. Lee, J. A. Gardener, A. J. Akey, R. Engelke, Y. Ronen, R. Zhong, G. Gu, S. Plugge, T. Tummuru, M. Kim, M. Franz, J. H. Pixley, N. Poccia, and P. Kim, Time-reversal symmetry breaking superconductivity between twisted cuprate superconductors, Science **382**, 1422 (2023).

[37] T. Li, S. Jiang, B. Shen, Y. Zhang, L. Li, Z. Tao, T. Devakul, K. Watanabe, T. Taniguchi, L. Fu, J. Shan, and K. F. Mak, Quantum anomalous Hall effect from intertwined moiré bands, Nature (London) **600**, 641 (2021).

[38] Y. Guo, J. Pack, J. Swann, L. Holtzman, M. Cothrine, K. Watanabe, T. Taniguchi, D. Mandrus, K. Barmak, J. Hone, A. J. Millis, A. N. Pasupathy, and C. R. Dean, Superconductivity in twisted bilayer WSe$_2$, arXiv:2406.03418.

[39] Y. Xia, Z. Han, K. Watanabe, T. Taniguchi, J. Shan, and K. F. Mak, Superconductivity in twisted bilayer WSe$_2$, Nature (2024).

[40] Z. Ji, H. Park, M. E. Barber, C. Hu, K. Watanabe, T. Taniguchi, J.-H. Chu, X. Xu, and Z.-x. Shen, Local probe of bulk and edge states in a fractional Chern insulator, arXiv:2404.07157.

[41] E. Redekop, C. Zhang, H. Park, J. Cai, E. Anderson, O. Sheekey, T. Arp, G. Babikyan, S. Salters, K. Watanabe, T. Taniguchi, X. Xu, and A. F. Young, Direct magnetic imaging of fractional Chern insulators in twisted MoTe$_2$ with a superconducting sensor, arXiv:2405.10269.

[42] R. Bistritzer and A. H. MacDonald, Moiré bands in twisted double-layer graphene, Proc. Natl. Acad. Sci. U.S.A. **108**, 12233 (2011).

[43] C. N. Lau, M. W. Bockrath, K. F. Mak, and F. Zhang, Reproducibility in the fabrication and physics of moiré materials, Nature (London) **602**, 41 (2022).

[44] Sayed Ali Akbar Ghorashi, A. Dunbrack, A. Abouelkomsan, J. Sun, X. Du, and J. Cano, Topological and stacked flat bands in bilayer graphene with a superlattice potential, Phys. Rev. Lett. **130**, 196201 (2023).

[45] Sayed Ali Akbar Ghorashi and J. Cano, Multilayer graphene with a superlattice potential, Phys. Rev. B **107**, 195423 (2023).

[46] Y. Zeng, T. M. R. Wolf, C. Huang, N. Wei, Sayed Ali Akbar Ghorashi, A. H. MacDonald, and J. Cano, Gate-tunable topological phases in superlattice modulated bilayer graphene, Phys. Rev. B **109**, 195406 (2024).

[47] C. Wang, X.-W. Zhang, X. Liu, Y. He, X. Xu, Y. Ran, T. Cao, and D. Xiao, Fractional Chern insulator in twisted bilayer MoTe$_2$, Phys. Rev. Lett. **132**, 036501 (2024).

[48] Z. Liu, E. J. Bergholtz, H. Fan, and A. M. Läuchli, Fractional Chern insulators in topological flat bands with higher Chern number, Phys. Rev. Lett. **109**, 186805 (2012).

[49] S. Yang, Z.-C. Gu, K. Sun, and S. Das Sarma, Topological flat band models with arbitrary Chern numbers, Phys. Rev. B **86**, 241112(R) (2012).

[50] Y.-F. Wang, H. Yao, C.-D. Gong, and D. N. Sheng, Fractional quantum Hall effect in topological flat bands with Chern number two, Phys. Rev. B **86**, 201101(R) (2012).

[51] A. Sterdyniak, C. Repellin, B. A. Bernevig, and N. Regnault, Series of Abelian and non-Abelian states in $C > 1$ fractional Chern insulators, Phys. Rev. B **87**, 205137 (2013).

[52] Y.-L. Wu, N. Regnault, and B. A. Bernevig, Bloch model wave functions and pseudopotentials for all fractional Chern insulators, Phys. Rev. Lett. **110**, 106802 (2013).

[53] M. Barkeshli and X.-L. Qi, Topological nematic states and non-Abelian lattice dislocations, Phys. Rev. X **2**, 031013 (2012).

[54] M. Barkeshli, C.-M. Jian, and X.-L. Qi, Twist defects and projective non-Abelian braiding statistics, Phys. Rev. B **87**, 045130 (2013).

[55] G. Möller and N. R. Cooper, Fractional Chern insulators in Harper-Hofstadter bands with higher Chern number, Phys. Rev. Lett. **115**, 126401 (2015).

[56] Y.-H. Wu, J. K. Jain, and K. Sun, Fractional topological phases in generalized Hofstadter bands with arbitrary Chern numbers, Phys. Rev. B **91**, 041119(R) (2015).

[57] J. Behrmann, Z. Liu, and E. J. Bergholtz, Model fractional Chern insulators, Phys. Rev. Lett. **116**, 216802 (2016).

[58] B. Andrews and G. Möller, Stability of fractional Chern insulators in the effective continuum limit of Harper-Hofstadter bands with Chern number $|C| > 1$, Phys. Rev. B **97**, 035159 (2018).

[59] J. Wang and Z. Liu, Hierarchy of ideal flatbands in chiral twisted multilayer graphene models, Phys. Rev. Lett. **128**, 176403 (2022).

[60] Z. Liu and E. J. Bergholtz, Recent developments in fractional Chern insulators, in *Encyclopedia of Condensed Matter Physics*, 2nd ed., edited by T. Chakraborty (Academic Press, Oxford, UK, 2024), pp. 515–538.

[61] E. Khalaf, S. Chatterjee, N. Bultinck, M. P. Zaletel, and A. Vishwanath, Charged skyrmions and topological origin of superconductivity in magic-angle graphene, Sci. Adv. **7**, eabf5299 (2021).

[62] S. Chatterjee, M. Ippoliti, and M. P. Zaletel, Skyrmion superconductivity: DMRG evidence for a topological route to superconductivity, Phys. Rev. B **106**, 035421 (2022).

[63] P. Törmä, S. Peotta, and B. A. Bernevig, Superconductivity, superfluidity and quantum geometry in twisted multilayer systems, Nat. Rev. Phys. **4**, 528 (2022).

[64] J. Sun, S. A. A. Ghorashi, K. Watanabe, T. Taniguchi, F. Camino, J. Cano, and X. Du, Signature of correlated insulator in electric field controlled superlattice, Nano Lett. (2024), doi:10.1021/acs.nanolett.4c03238.

[65] C. R. Dean, L. Wang, P. Maher, C. Forsythe, F. Ghahari, Y. Gao, J. Katoch, M. Ishigami, P. Moon, M. Koshino, T. Taniguchi, K. Watanabe, K. L. Shepard, J. Hone, and P. Kim, Hofstadter's butterfly and the fractal quantum Hall effect in moiré superlattices, Nature (London) **497**, 598 (2013).

[66] A. T. Pierce, Y. Xie, J. M. Park, E. Khalaf, S. H. Lee, Y. Cao, D. E. Parker, P. R. Forrester, S. Chen, K. Watanabe, T. Taniguchi, A. Vishwanath, P. Jarillo-Herrero, and A. Yacoby, Unconventional sequence of correlated Chern insulators in

[67] Y. Saito, J. Ge, L. Rademaker, K. Watanabe, T. Taniguchi, D. A. Abanin, and A. F. Young, Hofstadter subband ferromagnetism and symmetry-broken Chern insulators in twisted bilayer graphene, Nat. Phys. **17**, 478 (2021).

[68] I. Das, C. Shen, A. Jaoui, J. Herzog-Arbeitman, A. Chew, C.-W. Cho, K. Watanabe, T. Taniguchi, B. A. Piot, B. A. Bernevig, and D. K. Efetov, Observation of reentrant correlated insulators and interaction-driven Fermi-surface reconstructions at one magnetic flux quantum per moiré unit cell in magic-angle twisted bilayer graphene, Phys. Rev. Lett. **128**, 217701 (2022).

[69] J. Herzog-Arbeitman, A. Chew, D. K. Efetov, and B. A. Bernevig, Reentrant correlated insulators in twisted bilayer graphene at 25 T (2π flux), Phys. Rev. Lett. **129**, 076401 (2022).

[70] J. Finney, A. L. Sharpe, E. J. Fox, C. L. Hsueh, D. E. Parker, M. Yankowitz, S. Chen, K. Watanabe, T. Taniguchi, C. R. Dean, A. Vishwanath, M. A. Kastner, and D. Goldhaber-Gordon, Unusual magnetotransport in twisted bilayer graphene, Proc. Natl. Acad. Sci. U.S.A. **119**, e2118482119 (2022).

[71] C. Forsythe, X. Zhou, K. Watanabe, T. Taniguchi, A. Pasupathy, P. Moon, M. Koshino, P. Kim, and C. R. Dean, Band structure engineering of 2D materials using patterned dielectric superlattices, Nat. Nanotechnol. **13**, 566 (2018).

[72] Y. Li, S. Dietrich, C. Forsythe, T. Taniguchi, K. Watanabe, P. Moon, and C. R. Dean, Anisotropic band flattening in graphene with one-dimensional superlattices, Nat. Nanotechnol. **16**, 525 (2021).

[73] D. Barcons Ruiz, H. Herzig Sheinfux, R. Hoffmann, I. Torre, H. Agarwal, R. K. Kumar, L. Vistoli, T. Taniguchi, K. Watanabe, A. Bachtold, and F. H. L. Koppens, Engineering high quality graphene superlattices via ion milled ultra-thin etching masks, Nat. Commun. **13**, 6926 (2022).

[74] E. McCann, Asymmetry gap in the electronic band structure of bilayer graphene, Phys. Rev. B **74**, 161403(R) (2006).

[75] E. McCann and V. I. Fal'ko, Landau-level degeneracy and quantum Hall effect in a graphite bilayer, Phys. Rev. Lett. **96**, 086805 (2006).

[76] A. H. Castro Neto, F. Guinea, N. M. R. Peres, K. S. Novoselov, and A. K. Geim, The electronic properties of graphene, Rev. Mod. Phys. **81**, 109 (2009).

[77] E. McCann and M. Koshino, The electronic properties of bilayer graphene, Rep. Prog. Phys. **76**, 056503 (2013).

[78] T. Ohta, A. Bostwick, T. Seyller, K. Horn, and E. Rotenberg, Controlling the electronic structure of bilayer graphene, Science **313**, 951 (2006).

[79] H. Min, B. Sahu, S. K. Banerjee, and A. H. MacDonald, *Ab initio* theory of gate induced gaps in graphene bilayers, Phys. Rev. B **75**, 155115 (2007).

[80] E. V. Castro, K. S. Novoselov, S. V. Morozov, N. M. R. Peres, J. M. B. Lopes dos Santos, J. Nilsson, F. Guinea, A. K. Geim, and A. H. Castro Neto, Biased bilayer graphene: Semiconductor with a gap tunable by the electric field effect, Phys. Rev. Lett. **99**, 216802 (2007).

[81] I. Martin, Y. M. Blanter, and A. F. Morpurgo, Topological confinement in bilayer graphene, Phys. Rev. Lett. **100**, 036804 (2008).

[82] F. Zhang, J. Jung, G. A. Fiete, Q. Niu, and A. H. MacDonald, Spontaneous quantum Hall states in chirally stacked few-layer graphene systems, Phys. Rev. Lett. **106**, 156801 (2011).

[83] H. Rokni and W. Lu, Layer-by-layer insight into electrostatic charge distribution of few-layer graphene, Sci. Rep. **7**, 42821 (2017).

[84] M. Eich, F. c. v. Herman, R. Pisoni, H. Overweg, A. Kurzmann, Y. Lee, P. Rickhaus, K. Watanabe, T. Taniguchi, M. Sigrist, T. Ihn, and K. Ensslin, Spin and valley states in gate-defined bilayer graphene quantum dots, Phys. Rev. X **8**, 031023 (2018).

[85] A. Kurzmann, M. Eich, H. Overweg, M. Mangold, F. Herman, P. Rickhaus, R. Pisoni, Y. Lee, R. Garreis, C. Tong, K. Watanabe, T. Taniguchi, K. Ensslin, and T. Ihn, Excited states in bilayer graphene quantum dots, Phys. Rev. Lett. **123**, 026803 (2019).

[86] Y. Lee, A. Knothe, H. Overweg, M. Eich, C. Gold, A. Kurzmann, V. Klasovika, T. Taniguchi, K. Wantanabe, V. Fal'ko, T. Ihn, K. Ensslin, and P. Rickhaus, Tunable valley splitting due to topological orbital magnetic moment in bilayer graphene quantum point contacts, Phys. Rev. Lett. **124**, 126802 (2020).

[87] A. Kurzmann, Y. Kleeorin, C. Tong, R. Garreis, A. Knothe, M. Eich, C. Mittag, C. Gold, F. K. de Vries, K. Watanabe, T. Taniguchi, V. Fal'ko, Y. Meir, T. Ihn, and K. Ensslin, Kondo effect and spin–orbit coupling in graphene quantum dots, Nat. Commun. **12**, 6004 (2021).

[88] D. Vanderbilt, *Berry Phases in Electronic Structure Theory: Electric Polarization, Orbital Magnetization and Topological Insulators* (Cambridge University Press, Cambridge, UK, 2018).

[89] E. Brown, Bloch electrons in a uniform magnetic field, Phys. Rev. **133**, A1038 (1964).

[90] J. Zak, Magnetic translation group, Phys. Rev. **134**, A1602 (1964).

[91] J. Zak, Magnetic translation group. II. Irreducible representations, Phys. Rev. **134**, A1607 (1964).

[92] J. Zak, Group-theoretical consideration of Landau level broadening in crystals, Phys. Rev. **136**, A776 (1964).

[93] J. Zak, Proper functions for a Bloch electron in a magnetic field, Phys. Rev. **139**, A1159 (1965).

[94] D. R. Hofstadter, Energy levels and wave functions of Bloch electrons in rational and irrational magnetic fields, Phys. Rev. B **14**, 2239 (1976).

[95] D. J. Thouless, M. Kohmoto, M. P. Nightingale, and M. den Nijs, Quantized Hall conductance in a two-dimensional periodic potential, Phys. Rev. Lett. **49**, 405 (1982).

[96] D. Xiao, M.-C. Chang, and Q. Niu, Berry phase effects on electronic properties, Rev. Mod. Phys. **82**, 1959 (2010).

[97] J. Herzog-Arbeitman, Z.-D. Song, N. Regnault, and B. A. Bernevig, Hofstadter topology: Noncrystalline topological materials at high flux, Phys. Rev. Lett. **125**, 236804 (2020).

[98] T. Ozawa and B. Mera, Relations between topology and the quantum metric for Chern insulators, Phys. Rev. B **104**, 045103 (2021).

[99] J. Wang, J. Cano, A. J. Millis, Z. Liu, and B. Yang, Exact Landau level description of geometry and interaction in a flatband, Phys. Rev. Lett. **127**, 246403 (2021).

[100] J. Herzog-Arbeitman, A. Chew, and B. A. Bernevig, Magnetic Bloch theorem and reentrant flat bands in twisted bilayer graphene at 2π flux, Phys. Rev. B **106**, 085140 (2022).

[101] X. Wang and O. Vafek, Narrow bands in magnetic field and strong-coupling Hofstadter spectra, Phys. Rev. B **106**, L121111 (2022).

[102] X. Wang and O. Vafek, Revisiting Bloch electrons in a magnetic field: Hofstadter physics via hybrid Wannier states, Phys. Rev. B **108**, 245109 (2023).

[103] Y. Fang and J. Cano, Symmetry indicators in commensurate magnetic flux, Phys. Rev. B **107**, 245108 (2023).

[104] K. Singh, A. Chew, J. Herzog-Arbeitman, B. A. Bernevig, and O. Vafek, Topological heavy fermions in magnetic field, Nat. Commun. **15**, 5257 (2024).

[105] J. Herzog-Arbeitman (private communication, 2023).

[106] X. Wang, J. R. Yates, I. Souza, and D. Vanderbilt, *Ab initio* calculation of the anomalous Hall conductivity by Wannier interpolation, Phys. Rev. B **74**, 195118 (2006).

[107] X. Wang, D. Vanderbilt, J. R. Yates, and I. Souza, Fermi-surface calculation of the anomalous Hall conductivity, Phys. Rev. B **76**, 195109 (2007).

[108] K. Nielsch, R. B. Wehrspohn, J. Barthel, J. Kirschner, U. Gösele, S. F. Fischer, and H. Kronmüller, Hexagonally ordered 100 nm period nickel nanowire arrays, Appl. Phys. Lett. **79**, 1360 (2001).

[109] K. Nielsch, R. B. Wehrspohn, J. Barthel, J. Kirschner, S. F. Fischer, H. Kronmüller, T. Schweinböck, D. Weiss, and U. Gösele, High density hexagonal nickel nanowire array, J. Magn. Magn. Mater. **249**, 234 (2002).

[110] P. Bruno, V. K. Dugaev, and M. Taillefumier, Topological Hall effect and Berry phase in magnetic nanostructures, Phys. Rev. Lett. **93**, 096806 (2004).

[111] M. Taillefumier, V. K. Dugaev, B. Canals, C. Lacroix, and P. Bruno, Chiral two-dimensional electron gas in a periodic magnetic field: Persistent current and quantized anomalous Hall effect, Phys. Rev. B **78**, 155330 (2008).

[112] U. Yaron, P. L. Gammel, A. P. Ramirez, D. A. Huse, D. J. Bishop, A. I. Goldman, C. Stassis, P. C. Canfield, K. Mortensen, and M. R. Eskildsen, Microscopic coexistence of magnetism and superconductivity in $ErNi_2B_2C$, Nature (London) **382**, 236 (1996).

[113] Y. De Wilde, M. Iavarone, U. Welp, V. Metlushko, A. E. Koshelev, I. Aranson, G. W. Crabtree, and P. C. Canfield, Scanning tunneling microscopy observation of a square Abrikosov lattice in $LuNi_2B_2C$, Phys. Rev. Lett. **78**, 4273 (1997).

[114] M. R. Eskildsen, P. L. Gammel, B. P. Barber, U. Yaron, A. P. Ramirez, D. A. Huse, D. J. Bishop, C. Bolle, C. M. Lieber, S. Oxx, S. Sridhar, N. H. Andersen, K. Mortensen, and P. C. Canfield, Observation of a field-driven structural phase transition in the flux line lattice in $ErNi_2B_2C$, Phys. Rev. Lett. **78**, 1968 (1997).

[115] M. Yethiraj, D. M. Paul, C. V. Tomy, and E. M. Forgan, Neutron scattering study of the flux lattice in YNi_2B_2C, Phys. Rev. Lett. **78**, 4849 (1997).

[116] S. P. Brown, D. Charalambous, E. C. Jones, E. M. Forgan, P. G. Kealey, A. Erb, and J. Kohlbrecher, Triangular to square flux lattice phase transition in $YBa_2Cu_3O_7$, Phys. Rev. Lett. **92**, 067004 (2004).

[117] C. Reichhardt and N. Grønbech-Jensen, Critical currents and vortex states at fractional matching fields in superconductors with periodic pinning, Phys. Rev. B **63**, 054510 (2001).

[118] Q. Han, Z. D. Wang, Q.-H. Wang, and T. Xia, Vortex state in $Na_xCoO_2 \cdot yH_2O$:$p_x \pm ip_y$–wave versus $d_{x^2-y^2} \pm id_{xy}$–wave pairing, Phys. Rev. Lett. **92**, 027004 (2004).

[119] Q. Meng, C. N. Varney, H. Fangohr, and E. Babaev, Honeycomb, square, and kagome vortex lattices in superconducting systems with multiscale intervortex interactions, Phys. Rev. B **90**, 020509(R) (2014).